Far-Field Superresolution Imaging via Spatial Frequency Modulation

Mingwei Tang, Xiaowei Liu, Zhong Wen, Feihong Lin, Chao Meng, Xu Liu,*
Yaoguang Ma,* and Qing Yang*

The diffraction limit substantially impedes the resolution of the conventional optical microscope. Under traditional illumination, the high-spatial-frequency light corresponding to the subwavelength information of objects is located in the near-field in the form of evanescent waves, and thus not detectable by conventional far-field objectives. Recent advances in nanomaterials and metamaterials provide new approaches to break this limitation by utilizing large-wavevector evanescent waves. Here, a comprehensive review of this emerging and fast-growing field is presented. The current superresolution imaging techniques based on evanescent-wave-assisted spatial frequency modulation, including hyperlens, microsphere lens, and evanescent field-illuminated spatial frequency shift microscopy, are illustrated. They are promising in investigating unobserved details and processes in fields such as medicine, biology, and material research. Some current challenges and future possibilities of these superresolution methods are also discussed.

1. Introduction

Optical microscopy is probably one of the most significant technical accomplishments in the history of humankind. Since its first invention by Hans Lippershey and Zacharias Janssen around 1590, optical microscopy has revolutionized many aspects of science and technology, especially in life sciences, for its superiorities in minimal invasiveness and excellent compatibility with live-cell imaging. However, classical linear optical microscopy is still restrained by the optical resolution limitation formulated by Abbe in his revolutionary paper published in 1873.[1] von Helmholtz derived a more general expression of this concept, that resolution under conventional illumination is described by the illumination wavelength (λ_0) and the numerical aperture (NA) of the

system: $R = \frac{\lambda_0}{2\,\mathrm{NA}}$.[2] The resolution of a traditional optical microscope (i.e., the smallest distance at which two point-like objects could be discriminated) under visible light illumination can only reach $\approx$200 nm in the lateral dimensions and $\approx$500 nm in the axial dimension using an objective lens (NA = 1.4) at 550 nm wavelength. These values are fundamentally restricted by optical diffraction (or uncertainty principle in the perspective of quantum physics), which leads to the absence of subwavelength information of the object. The increasing demand for improved resolution has been inspiring numerous attempts to break the resolution limit. However, it was not until recently that fruitful developments emerged. In this review, we focus on the discussion of lateral superresolution microscopy.

The confocal laser scanning microscopy (CLSM) invented in the 1960s utilizes focused laser for excitation and a pinhole for detection to shape the point-spread function (PSF) of the system and increases the resolution of a microscope down to around $1/\sqrt{2}$ of the diffraction limit.[3–5] The combination of CLSM and fluorescent microscopy has become a powerful indispensable tool for life science and material science since its invention.[6]

By further advancing the confocal system, superresolution fluorescent microscopy circumvents the diffraction limit by distinguishing the fluorescent emission of different areas or fluorophores in an additional dimension, e.g., spectroscopic characteristics or time.[7] Reversible saturable optical fluorescence transitions (RESOLFT) microscopy represents a typical class of this absolute far-field strategy, which reversely silences fluorophores at the predefined diffraction-limited region and shrink the PSF.[8–14] Several newly invented methods share this principle, e.g., stimulated emission depletion (STED) microscopy,[8,10] ground state depletion (GSD) microscopy,[15,16] saturated pattern excitation (SPE) microscopy,[17] and dynamic saturation optical microscopy (DSOM).[18] Another category of the method relies on the precise location of the single emitter by activating individual molecules stochastically within the diffraction-limited region at different time intervals. Such single-molecule localization microscopy (SMLM) includes stochastic optical reconstruction microscopy (STORM),[19,20] photoactivated localization microscopy (PALM),[21] and fluorescence photoactivation localization

Dr. M. Tang, Dr. X. Liu, Dr. Z. Wen, Dr. F. Lin, Dr. C. Meng, Prof. X. Liu, Prof. Y. Ma, Prof. Q. Yang
State Key Laboratory of Modern Optical Instrumentation, College of Optical Science and Engineering
Zhejiang University
Hangzhou 310027, China
E-mail: liuxu@zju.edu.cn; mayaoguang@zju.edu.cn; qingyang@zju.edu.cn
Prof. Q. Yang
Collaborative Innovation Center of Extreme Optics
Shanxi University
Taiyuan 030006, China

The ORCID identification number(s) for the author(s) of this article can be found under https://doi.org/10.1002/lpor.201900011

1900011 (1 of 22)

**ADVANCED
SCIENCE NEWS**

www.advancedsciencenews.com

LASER
& PHOTONICS
REVIEWS

www.lpr-journal.org

microscopy (FPALM), etc.[22] The method mentioned above relies heavily on special fluorescent markers, thus limits their employment in label-free and fluorescent-probe-limited scenarios.[23–25] A detailed description of these methods will not be covered in this paper and can be found in other reviews.[26–33] Another intriguing attempt worth noting is to employ the carefully designed amplitude or phase zone plate to achieve subdiffraction-limit focusing in the far-field, that is so called superoscillatory lens.[34–38] Through the judiciously designed diffractive unit, the focal spot size in a certain region of the target plane is controllable in lateral (from infinite small to $0.38\ \lambda/\text{NA}$) [39] and longitudinal directions.[40] Combined with the confocal technique, both labeled and label-free superresolution microscopy could be realized in a purely noninvasive manner.[34,40,41] However, the decreased focus spot is usually accompanied by increased sidelobes, which imposes practical difficulties in its applications in superresolution imaging. For more information on this planer diffractive lens, please refer to the latest reviews.[35,42]

To enhance the lateral resolution in far-field microscopy without the slow scanning process, people innovatively turn to manipulation in the spatial frequency (SF) domain instead of the spatial domain. This method, termed as spatial frequency modulation (SFM), can realize a high-speed and wide-field high-resolution imaging. The classical technique is structured illumination microscopy (SIM), which uses the Moiré effect to improve the imaging resolution by illuminating the sample with patterned light.[43–46] Limited by the pattern periodicity realized by the interference of two free-space light, the lateral resolution can only reach down to $\approx\lambda/4$. Another way of increasing the resolution is Fourier ptychographic microscopy (FPM),[47–49] which recovers high-resolution images from multiple low-resolution images taken under oblique illuminations.[50–52] By shifting the high spatial-frequency information into the collectible area in the SF space defined by the objective NA, these methods operate in SF space stitching together several variably illuminated low-resolution images. Although these methods have many advantages including low illumination density, good biocompatibility, simple sample preparation process, fast imaging speed and wide field of view (FOV) compared with other superresolution imaging methods,[7,53–59] deep-subwavelength superresolving ability was not provided due to the limited spatial-frequency-shift range restricted by free-space light illumination. Thus, evanescent wave illumination, instead of free-space light, is necessary to further break the diffraction limit in order to cover larger spatial-frequency range in the SF space.

Evanescent waves were first employed by the microscopy community in the 1940s.[60] The in-plane wavevector of an evanescent wave is larger than that of a propagating wave and corresponds to finer details of the object. In other words, the subdiffraction-limited details could be visualized once evanescent waves are collected. Near-field scanning optical microscopy (NSOM) is the first technique invented to capture the evanescent waves in the near-field region, which uses the nanometer-sized probes to scan point by point and collect the corresponding evanescent waves on the specimen's surface.[61–69] However, this technique has relatively low throughput and requires post-processing of massive scanning data. In the past decades, a series of superresolution techniques exploiting SF modulation of evanescent waves have been reported, including hyperlens[70–77] and microsphere lens.[78–96] These methods enable the one-shot collection of evanescent waves via spatial frequency compression (SFC) method to transform large-wavevector evanescent waves into propagating light. Besides the SFC method, superresolution microscopy also benefits from evanescent wave illumination combined with spatial frequency shift (SFS) method. Generally speaking, superresolution microscopy utilizes mainly two kinds of evanescent waves for illumination, evanescent fields at dielectric waveguide boundaries,[97] and surface plasmon polaritons (SPPs) or localized plasmons (LPs) at metal/dielectric interfaces.[98,99] Several papers have reported evanescent-wave-assisted SFS methods using delicately designed structures, including evanescent fields illuminated SFS label-free microscopy,[51,100] evanescent fields illuminated SFS labeled microscopy,[101,102] plasmonic structured illumination microscopy (PSIM),[52,103–105] and localized plasmonic structured illumination microscopy (LPSIM).[106,107]

This review aims to provide a systematic discussion on the evanescent-wave-assisted SFM superresolution microscopy techniques (**Figure 1**) since other reviews only have covered parts of this promising research area.[50,108–110] A summary of the principles, developments, features, performances of different superresolution techniques is listed in **Table 1**. It should be noted that some techniques, such as nonlinear effects are beyond the scope of this paper, although they are very prospective methods that can fundamentally break the diffraction limit.[44,46]

2. Principles of Superresolution Imaging by SFM

The foundation of superresolution imaging by SFM lies in the collection of evanescent waves in the near-field region of the specimen's surface. A perfect optical imaging process can be described as the collection of an infinite number of plane waves with different spatial frequencies ranging from $-\infty$ to ∞. When an object $O(x, y, z)$ in the plane of $z = z_0$ was illuminated by a plane wave vertically, the electrical amplitude in the plane can be expressed in Equation (1)

$$E\left(x, y\right) = \iint\limits_{-\infty}^{\infty} F\left(f_x, f_y\right) e^{i\left(2\pi f_x x + 2\pi f_y y\right)} df_x df_y \tag{1}$$

where $F(f_x, f_y)$ represents the spatial spectrum of the object in the lateral directions. Waves with lateral spatial frequencies $(2\pi f_x)^2 + (2\pi f_y)^2 > \frac{2\pi}{\lambda}$ correspond to the evanescent waves as they can only locate in the near-field region and decay exponentially in the z-direction. It follows that the lateral component of the evanescent wave will be larger than a propagating wave and corresponds to the information of finer details. A conventional microscope acts as a low-pass SF filter that detects the light signal limited by its NA

$$F(\vec{k}) = F_o(\vec{k}) \cdot TF(\vec{k}) \tag{2}$$

where $\vec{k} = (2\pi f_x, 2\pi f_y)$ represents the spatial frequency in the lateral plane, $F_o(\vec{k})$ and $TF(\vec{k})$ are the Fourier spectrum of the object and the transfer function (TF) of the imaging system. Here,

**ADVANCED
SCIENCE NEWS**

www.advancedsciencenews.com

LASER
& PHOTONICS
REVIEWS

www.lpr-journal.org
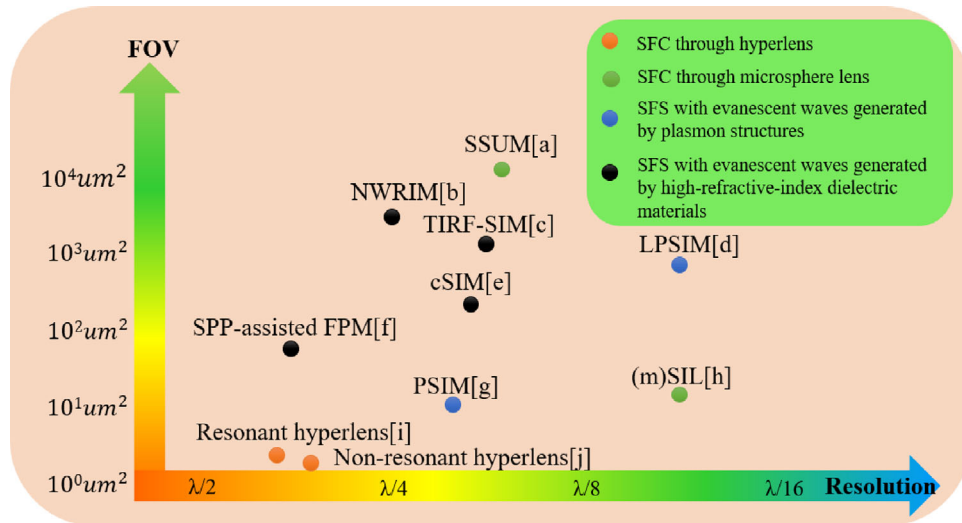
Figure 1. Experimental demonstration of the evanescent-wave-assisted SFM superresolution microscopy techniques discussed in this review. The FOV and the resolution of hyperlens, microsphere lens, evanescent fields illuminated SFS microscopy, and PSIM are compared in this diagram. (a–j) correspond to refs. [79,51,205,107,102,48,103,81,70,71].

$\text{TF}(\vec{k})$ is a circular filter centered at 0 with a radius of $k_0 = \frac{2\pi \text{NA}}{\lambda}$ for coherent imaging and $k_0 = \frac{4\pi \text{NA}}{\lambda}$ for incoherent imaging. Thus, large-wavevector waves, especially the evanescent waves, cannot be collected by objectives. This filtering effect leads to a loss of finer-detail information and hence the diffraction limit, as shown in **Figure 2**, where the blue circle represents the detected SF domain of a diffraction-limited microscope. In the imaging media with a refractive index of *n*, the theoretical resolution limit is $\frac{\lambda}{2n}$. SFM method was then proposed to overcome the low-pass filtering effect. This method can be mainly categorized into two groups: SFC method and SFS method.

2.1. Principle of SFC Method

The SFC method uses a near-field-contacting lens to adiabatically compress the wavevector of evanescent waves on the specimens' surface. The imaging process involves collecting the near-field large-wavevector evanescent waves and converting it into propagating waves, which, in the view of imaging, provides magnified images of the objects. Therefore, an ordinary microscope objective lens could pick up the magnified images and discern the subdiffraction-limited structures. In other words, the spatial spectra of objects are compressed to fit the observable region of the imaging system, as depicted in Figure 2a. In this case, the detected spatial spectrum of the objects can be described as

$$F_{\text{fc}}(\vec{k}) = F_{\text{o}}(\overrightarrow{Mk}) \cdot \text{TF}(\vec{k}) \qquad (3)$$

where $\vec{k}$ represents the spatial frequency, $F_{\text{o}}(\vec{k})$ and $\text{TF}(\vec{k})$ are the Fourier spectra of the object and the TF of the imaging system, *M* is the compression factor of the spatial frequency. And the resolution of SFC methods is $R_{\text{fc}} = \frac{2\pi}{M k_{\text{c}}}$, k_{c} is the cutoff spatial frequency of the optical system.

2.2. Principle of SFS Method

On the other hand, for SFS methods, evanescent wave illumination provides a significant spatial frequency shift of the object's spatial spectrum, as shown in Figure 2b.

The detected spatial spectrum of objects can be described in a similar way

$$F_{\text{fs}}(\vec{k}) = F_{\text{o}}(\vec{k} - \vec{k}_{\text{s}}) \cdot \text{TF}(\vec{k}) \qquad (4)$$

where $F_{\text{o}}(\vec{k})$, $\text{TF}(\vec{k})$ are the Fourier spectrum of the object and the TF of the imaging system, $\vec{k}_{\text{s}}$ is the spatial frequency shift provided by the evanescent-wave illumination. It should be noted that the TF should be adapted to optical transfer function (OTF) or coherent transfer function (CTF) in different imaging systems, e.g., we use the CTF in evanescent fields illuminated SFS label-free microscopy, while in the case of evanescent fields illuminated SFS labeled microscopy we use the OTF. As shown in Figure 2b, the spatial spectrum centered by $\vec{k}_{\text{s}}$ will be shifted to the lower SF region and transferred to propagating modes, thereby presenting superresolution information to the far-field. The final resolution of SFS methods is then $R_{\text{fs}} = \frac{2\pi}{k_{\text{c}} + k_{\text{s}}}$.

It should be noted that SFC and SFS methods differ in their imaging process. While the SFC method provides a one-shot imaging process, the SFC-based lenses are usually tiny (in micrometer scale) and require a scanning technique to obtain a large FOV. The SFS method could obtain a large FOV while it requires iterations of the shifted spectrum repeatedly in the SF space. With the development of powerful computers and advanced algorithms, the SFS iteration speed could be accelerated, and high frame-rate imaging can be achieved.

2.3. Quantifying the Resolution

The definition of the spatial resolution appears to be a little ambiguous among some reported papers and should be identified

Table 1. Summary of the principles, features, performances of different superresolution techniques introduced in this review. Notation: MRF, minimally resolved features.

Category	Technique	Lateral resolution [nm]	FOV [µm²] or speed [µm² min⁻¹]	Label fluorophore	Detection mode	Data processing	Limitation	Ref.
Near-field	NSOM	$\approx 1-120$	16 µm²	No need	Scanning	Need	Low throughput	[63,66–69]
	Superlens	60–145	≈ 23µm²	No need	Wide-field	No need	Near-sighted	[251,301]
PSF engineering	STED	10–80	≈ 126µm² s⁻¹	Restricted	Scanning	Need	Strong light illumination	[302]
	Superoscillatory lens	65 ($\lambda/6$)	0.36 µm² min⁻¹	No need	Scanning	Need	Slow scanning	[40]
SMLM	STORM、PALM、FPALM	10–50	169−2500 µm² (31 ms–40 s)	Restricted	Wide-field	Need	Restricted fluorescent probes	[303]
Nonlinear SIM	SSIM	≈ 50	≈ 700 µm²	Restricted	Wide-field	Need	Strong light illumination	[44]
	NL-SIM	42	≈ 1000µm²	Restricted	Wide-field	Need	Restricted fluorescent probes	[46]
SFC method	Resonant hyperlens	160($\lambda/2.6$)	≈ 1 µm²	No need	Wide-field	No need	Resolution is limited by a material loss in metal; small FOV	[70]
	Nonresonant hyperlens	250($\lambda/3.1$)	–	No need	Wide-field	No need	Small FOV	[71]
	Wide-field microsphere	50($\lambda/14-\lambda/8$) MRF	≈ 0.1 µm²	No need	Wide-field	No need	Small FOV	[88]
	(m)SIL microsphere	45($\lambda/10.4$) MRF	≈ 33µm²	No need	Wide-field	No need	Small FOV	[81]
	Scanning superlens microscopy (SSUM)	87($\lambda/6.3-\lambda/8.4$) 2D convolution	≈ 3000 µm² min⁻¹	No need	Wide-field and scanning	Need	Complex configuration	[79]
SFS method	SPP-based FPM	240 ($\lambda/2.7$) Period of gratings	≈ 80 µm²	No need	Wide-field	Need	Optical propagation loss	[48]
	Evanescent fields illuminated FPM	≈ 120($\lambda/4.3$)	≈ 6000 µm²	No need	Wide-field	Need	The refractive index of the waveguide limits the resolution.	[51,119]
	(TIRF-) SIM	80–130($\lambda/4-\lambda/6$)	≈ 2000 µm²	Broad	Wide-field	Need	Restricted resolution	[205]
	cSIM	55–117 ($\lambda/5.6-\lambda/10$)	≈ 400 µm²	Broad	Wide-field	Need	Complex chip fabrication	[102]
	PSIM	≈ 120($\lambda/4.8$)	≈ 20 µm²	Broad	Wide-field	Need	Optical propagation loss	[103]
	LPSIM	≈ 50 ($\lambda/11$)	≈ 800 µm²	Broad	Wide-field	Need	Complex chip fabrication	[106,107,200]

before we introduce various microscopies. Traditionally, the resolution was determined by using the classical resolution theory. Since the objective lens behaves like a circular aperture, the image of a point source passing through will appear as a central brightest disk (airy disk) accompanied by concentric rings. The size of the airy disk determines the actual resolution. According to the Rayleigh criterion, the resolution for the imaging system can be described by the distance from the central maximum of the PSF to its first root.[111] Practically, due to the difficulty of determining the minimum of the intensity diffraction pattern in Rayleigh's definition, the full width at half-maximum (FWHM) of the PSF can, in a sense, be used to define the resolution of the actual system. The detected pattern in the image space could be described as the convolution between the object and the imaging system's PSF

$$I(x, y) = \iint\limits_{-\infty}^{\infty} O(u, v)\, \mathrm{PSF}\left(\frac{x}{M} - u, \frac{y}{M} - v\right) du\, dv \tag{5}$$

where I, O are the image and object described in the two dimensions, M is the magnification factor of the imaging system.

In labeled microscopy, the detected images are emission intensity distribution of the fluorescent markers, which can be considered as independent point sources. The collected image of a single point source is determined as the optical system's PSF. The resolution can be easily determined by using the minimum central distance between two points or the FWHM of a single emitting point.

Compared with labeled imaging, the quantification of resolution in label-free imaging is more complicated due to the lack of suitable "point" sources. The mechanisms of label-free imaging rely on subtler light-scattering processes in nanoplasmonic or biomedical objects that result in lower sufficient contrast of images. Several experimental quantification methods have been reported in the literature to determine the resolution in their label-free microscopy systems. One method relies on the assumption that the resolution of a microscope can be

ADVANCED
SCIENCE NEWS
www.advancedsciencenews.com

LASER
& PHOTONICS
REVIEWS

www.lpr-journal.org
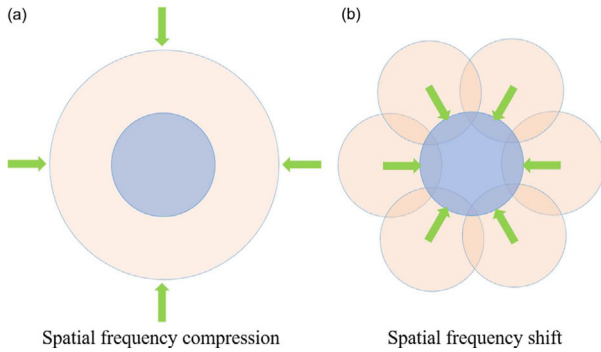
Figure 2. Mechanisms of evanescent-wave-assisted SFM method. a) SFC methods compress the spatial spectrum of objects using a specially designed lens. Thus a conventional objective can detect more subdiffraction-limited details. The blue circle represents the SF space detected by the conventional objective, while the orange one represents the SF space detected by the SFC method. b) SFS methods shift the high spatial spectrum of objects step by step to the detectable region of the objective and stitch them together in the SF space with the reconstruction algorithm. The blue circle represents the SF space detected by the conventional objective, while the orange one represents the SF space detected by the SFS method.

determined as the minimal spatial feature that it can be discerned, which are usually represented by the edge-to-edge gap of closely spaced nanodimers,[92,96,112,113] diameters of nanocylinders (or holes),[88,89] width of nanolines.[88,95,112,114–116] Although this method is straightforward, it usually results in overestimated resolution values, mainly because the sizes of these nanostructures are not small enough to be discerned as the point sources. Fabricating nanostructures with reduced dimensions is one possible solution but also leads to decreased optical contrast and visibility, which is harmful to the resolution quantification.

Instead, the center-to-center distance of nanodots or nanogratings could be used, which is more rigorous compared with the edge-to-edge gaps. This method has been demonstrated in the experiment to agree with the PSF theory result.[51,100,117–119]

Very recently, some reports exploit Equation (5) to inversely calculate the PSF of the label-free imaging system,[86,120,121] for example in microsphere lens imaging, in which the integration is performed in the object plane where the coordinates (x_o, y_o) are linearly related to the image plane via the magnification M as $(x_o, y_o) = (x_i/M, y_i/M)$. The Gaussian function is used to describe the PSF (x_o, y_o), with the FWHM being a fitting parameter. Based on the Houston criterion,[122] fitted values of FWHM in the object plane are considered as the resolution of the system.

3. Superresolution Imaging Based on SFC Methods

One direct approach to enhance the resolution is using the immersion technique to extend the NA of the imaging lens, which, however, is restrained by the low refractive index of natural materials.[123] The developments of metamaterials and nanofabrication techniques enable new opportunities for sophisticated lens design to increase the NA and, thus, resolution improvement.[50,108,124–127] Among these different lenses, hyperlens and microsphere lens are mostly studied. In this section, we will mainly discuss the theory underlying, as well as recent advances of these two kinds of superresolution microscopy.

3.1. SFC through Hyperlens

Hyperbolic metamaterial (HMM) is a kind of metamaterial with hyperbolic dispersion relationship, that is $\varepsilon_x = \varepsilon_y$ and ε_z taking opposite signs.[127,128] Their hyperbolic anisotropic dispersion naturally supports large wavevector components. One of the most prominent applications of HMM is the hyperlens,[127,129] which usually takes the form of concentrically curved layers bent from a stack of flat layers.

The dispersion of electromagnetic wave in HMM with curved geometry can be expressed in cylindrical coordinates by

$$\frac{k_\rho^2}{\varepsilon_\theta} + \frac{k_\theta^2}{\varepsilon_\rho} = \frac{\omega^2}{c^2} \tag{6}$$

where, k_ρ and k_θ are wavevectors, ε_ρ and ε_θ represent the permittivity along the radial and tangential directions, ω is the angular frequency, and c is the speed of light in the vacuum. For hyperlens with $\varepsilon_\rho \langle 0 \text{ and } \varepsilon_\theta \rangle 0$, the dispersion becomes $\frac{k_\rho^2}{\varepsilon_\theta} - \frac{k_\theta^2}{|\varepsilon_\rho|} = \frac{\omega^2}{c^2}$. This hyperbolic dispersion essentially determines that evanescent waves with large wavevector could be transferred along the radial direction in a hyperlens due to the unbounded wavevector values or very large wavevector cutoff. The accessible range k_θ, which determines the imaging resolution, could extend to a broader range compared with the isotropic case where the maximum of k_θ is restricted by the refractive index of the material. The curved geometry results in the compression of k_θ due to the conservation of angular momentum, thus a magnified image will be formed at the outer boundary. In other words, the high-spatial-frequency information, which is undetectable for conventional objectives, can now be transferred to low SF space and resolved in the far-field. The compression factor M is the radii ratio between the outer surface and the inner surface of the hyperlens. To realize a working hyperlens, subwavelength metal-dielectric multilayered metamaterials, i.e., plasmonic multilayers, are perfect options.[130] When the layer thickness is much smaller than the probing wavelength, the effective permittivity of the medium can be calculated as: $\varepsilon_\theta = p\varepsilon_m + (1-p)\varepsilon_d$, $\varepsilon_\rho = \frac{\varepsilon_m \varepsilon_d}{(1-p)\varepsilon_m + p\varepsilon_d}$, where ε_m and ε_d are the permittivity of metal and dielectric, p is the filling ratio of the metal.[131]

The most commonly used design to realize hyperlens is a concentric-ring multilayer structure, including the cylindrical/spherical/planer multilayer configurations. The cylindrical structure is the first experimental implement of hyperlens but limited to one-dimensional (1D) superresolution imaging (**Figure 3**a).[76] The spherical structure was designed and realized for two-dimensional (2D) superresolution in visible frequency (Figure 3b).[70] However, general imaging samples are not compatible with curved structures. As an alternative, planar configurations were proposed with parallel planes by using transformation optics techniques (Figure 3c).[75] This scheme has not been experimentally demonstrated, mainly due to the complexity of fabrication. One limitation of these previously implemented hyperlenses is the requirement of the curved geometry, which limits the imaging FOV. Besides, to realize a significant SF compression, the large radius ratio is required, which will inevitably lead to low transmission efficiency for the existence of material loss.
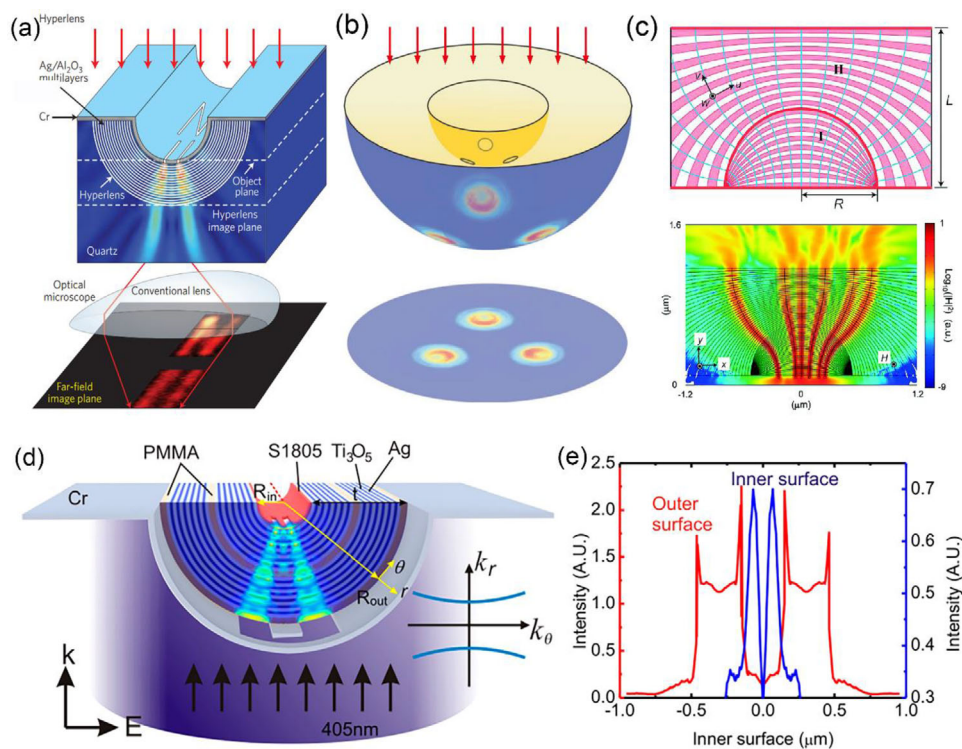
Figure 3. Typical configurations and spatial frequency compression principle of hyperlenses. a) Cylindrical configurations. The high spatial-frequency fields of the sample propagate along the radial direction of the hyperlens. Due to the conservation of angular momentum, these high spatial-frequency fields will be compressed, forming the magnified image on the other side of the hyperlens, which could be discerned by the conventional objective. Reproduced with permission.[76] Copyright 2007, Springer Nature. b) Spherical configurations. Reproduced with permission.[70] Copyright 2010, Springer Nature. c) Planar configurations. Reproduced with permission.[75] Copyright 2008, American Chemical Society. d) The demagnification hyperlens system applied in photolithography. e) Intensity distributions at the outer surface right after the mask (red) and inner surface inside the photoresist (blue) obtained in numerical simulations, as indicated in (d). (c,d) Reproduced with permission.[140] Copyright 2017, American Chemical Society.

To compensate for the material loss and further improve the resolution, the idea of active HMM has been proposed.[132] Theoretical studies have predicted the resolution improvement of hyperlens using organic dyes to compensate for the propagation loss.[132,133] Another direction to surmount the material loss is designing the new structure. Different from the concentric-ring multilayer hyperlenses relying strongly on the resonance and leading to limited bandwidth and high losses, another successful structure with negative permittivity along with the metal layers and positive permittivity in the perpendicular direction circumventing this problem was proposed.[134–136] Based on this principle, a nonresonant waveguide-integrated hyperlens with a radially oriented layered structure working in a longer wavelength of 780 nm was designed. The inner and outer radii of the hyperlens are 800 and 2400 nm, respectively, enabling three times magnification. Using this design, two nanoslits in the gold blocking layer with 250 nm center-to-center separation was experimentally resolved.[71] This nonresonant nature endows this hyperlens a low-loss performance in the visible frequency.

To circumvent the material loss and small FOV of hyperlens, another method based on the structured illumination from type II planer HMM, also termed as hyperstructured illumination microscopy (HSIM), was proposed by Narimanov in 2016.[137] The HSIM uses the strong material dispersion inherent to this kind of HMM to sweep the entire object plane. The subwavelength

localization of the electromagnetic field near the object and a dramatic difference in the intensity distribution for different wavelengths allow us to resolve distinct details of the specimen despite their close spacing. The ultimate spatial resolution of HSIM is limited by the unit pair size of the layer of HMM, which has been demonstrated to reach the scale of a few nanometers using epitaxial growth technique. Therefore, the HSIM method has the potential to resolve sub-10 nm structures, to the point of resolving large individual molecules, which is essential for biological and material sciences.

In 2018, Ma et al.[138] experimentally demonstrated the hyperstructured illumination by using an Ag/SiO$_2$ multilayer HMM. With a pair of nanoslits as a point source on HMM, the HMM can perform a 1D mapping from spatial locations in a subdiffraction scale to a spectrum. The far-field-collected spectral data were used to reconstruct superresolution images, achieving a resolution of ≈84 nm (the center-to-center distance), which is far beyond the diffraction limit (0.61 λ/NA: from 561 to 854 nm).

Apart from superresolution imaging, hyperlens could also be used to demagnify a diffraction-limited mask down to the subwavelength scale according to the reciprocity theorem (Figure 3d,e).[139,140] The demagnifying effect of hyperlens was demonstrated experimentally in 2016.[141] A cylindrical hyperlens constituted by 13 alternating layers of Ag (30 nm) and Ti$_3$O$_5$ (30 nm) was fabricated in this work, generating a pattern

**ADVANCED
SCIENCE NEWS**

www.advancedsciencenews.com

LASER
& PHOTONICS
REVIEWS

www.lpr-journal.org
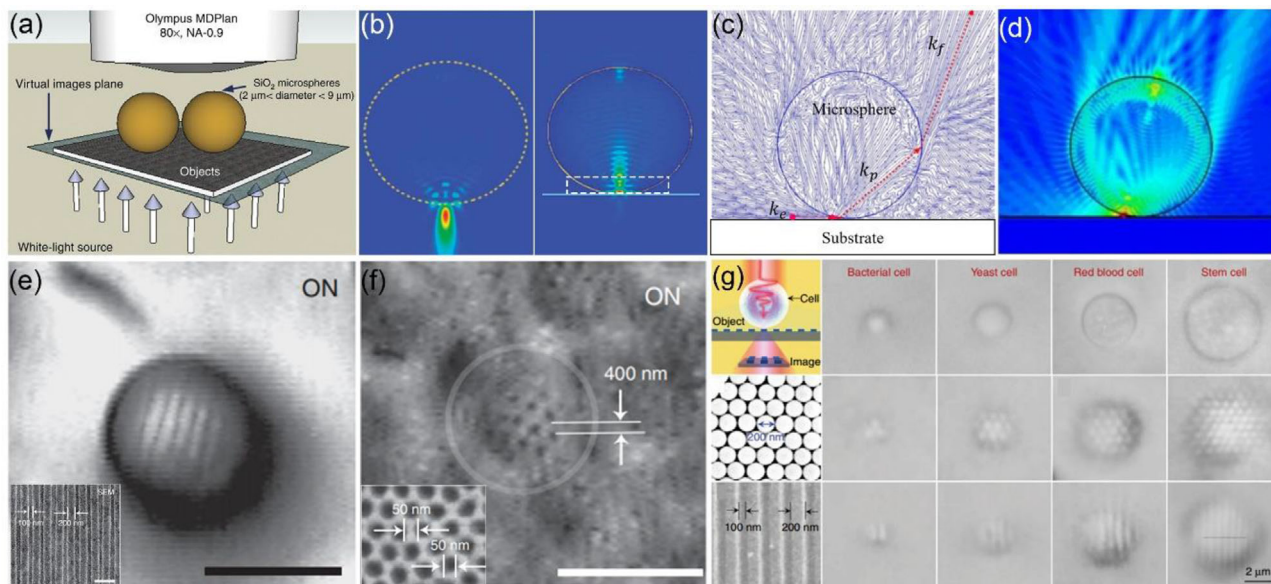
Figure 4. Configurations of microsphere nanoscopy. a) Direct imaging configuration. b) The intensity distributions calculated for the sphere (left image) and particle on the surface (right image) of a 40 nm thick gold film for the sphere with radius $a = 2.37$ μm and refractive index $n = 1.46$ at the wavelength $\lambda = 600$ nm. With the presence of a substrate, the focus at the particle-substrate contact region generally becomes sharper. The white dash rectangle shows the evanescent-wave contacting region. c) Calculated distribution of Poynting vector for a SiO_2 particle on a glass substrate. The particle size is 4.7 μm and the incident radiation wavelength $\lambda = 600$ nm. d) Distribution of the light intensity in the same situation as (c). (a–d) Reproduced with permission.[145] Copyright 2016, The Royal Society of Chemistry. e) Microsphere superlens reflection mode imaging of a commercial Blu-ray DVD disk. The subdiffraction-limited 100 nm lines (top left SEM image) are resolved by the microsphere superlens ($a = 2.37$ μm). f) Microsphere superlens transmission mode imaging of a gold-coated fishnet AAO sample with a microsphere superlens ($a = 2.37$ μm, borders of two spheres are shown by white lines). The nanoscope clearly resolves the pores that are 50 nm in diameter and spaced 50 nm apart (top left SEM image). Scale bar, 5 μm. (e,f) Reproduced with permission.[88] Copyright 2011, Springer Nature. g) Experimental imaging performance of different biomagnifiers. Reproduced with permission.[116] Copyright 2019, Springer Nature.

featuring around 170 nm (300 nm linewidth milled on the outside of the hyperlens) in the photoresist layer inside the hyperlens.

Although with the ability to realize far-field superresolution in a single shot, hyperlens superresolution microscopy still has a long way toward practical applications. First, the nanometer accuracy in controlling both thickness and geometric shape during the deposition of alternating metal and dielectric films of hyperlens requires complex and expensive fabrication processes. Second, to effectively collect the evanescent waves scattered by the observed object, the sample should be placed at specific positions in the active imaging region and near the surface of the hyperlens, which substantially restricts the preparation process of observed samples. In previously demonstrated experiments, the observable patterns are inscribed on the surface of hyperlens, which is unrealistic for practical application. Third, the hyperlens also has the shortcoming of small-batch fabrication. Recently, nanoimprint lithography has been applied in the fabrication of hyperlens arrays and realized a high-throughput subdiffraction-limited imaging system.[72,73]

3.2. SFC through Microsphere Lens

Aside from hyperlens configurations, the microsphere lens has also been demonstrated as an appropriate tool for superresolution imaging using the SFC method. In microsphere nanoscopy,

micrometer-scale spheres are placed on top of the target sample, where they collect the underlying sample's near-field large-wavevector evanescent information and form magnified images that are subsequently projected to the conventional objective lens. The combination of a microscope's objective lens and a microsphere lens forms a compound-imaging lens system, as illustrated in **Figure 4**a. Microsphere nanoscopy has distinct features of easy to implement, label-free, and supporting white light illumination.[79,84,89,142] Experiments show that it can resolve ≈50 nm features under white light illumination, which corresponds to a calibrated resolution of $\approx \frac{\lambda}{6} - \frac{\lambda}{8}$ based on rigorous PSF convolution.[86,121]

Attempts are trying to clarify the superresolution principle of the microsphere lens, but theories fully explaining this phenomenon remain controversial. Although the underlying details are still vague, we can understand the microsphere-based superresolution imaging qualitatively from a classical optics' perspective.[143] The microsphere lens effectively interacts with the near-field evanescent waves, decouples, compresses their wavevectors, and then turns them into propagating waves that would reach the objective lens in the far-field (Figure 4c,d).[108,144–146] Here the wavevectors satisfy: $k_e > k_p \geq k_f$, where k_e is the wavevector of sample's evanescent wave, k_p is wavevector of propagating waves in the microsphere lens, and k_f is the wavevector of propagating waves in the far-field. Compared with the case of merely using the objective lens, an objective lens combined with a microsphere lens can obtain both the high- and

ADVANCED
SCIENCE NEWS
www.advancedsciencenews.com

LASER
& PHOTONICS
REVIEWS

www.lpr-journal.org

low-spatial frequency of the sample simultaneously, i.e., an enlarged image with resolution better than the optical diffraction limit.

In the early experiments, the resolution was quantified using the semiquantitative resolution criteria, i.e., the minimum feature size that can be resolved.[88,92,113] However, this approach can provide overestimated resolution values, claiming about $\frac{\lambda}{8} - \frac{\lambda}{17}$[88,92] or even $\frac{\lambda}{25}$.[113] Therefore, a more rigorous quantification method was developed by inversely calculating the PSF of the superresolution imaging process, as stated in Section 2.3. For example, in Allen's work, they used the microsphere lens to image bowties with a gap of 15 nm.[86] With the more rigorous resolution quantification method, the resolution of this system should be determined as 74 instead of 15 nm.

3.2.1. Theories Underlying the Superresolving Capability of the Microsphere Lens

During the past years, scientists have come up with several theories attempting to account for this peculiar phenomenon. Nevertheless, other yet unknown factors are still needed to fully understand the process.[108,147,148]

Nanojet Explanation: Microsphere can focus light beyond the diffraction limit forming the so-called "nanojet" (Figure 4b).[80,149–152] For a long time, the theoretical explanation of the superresolution ability of the microsphere lens was based on a notion that focusing and imaging are fundamentally related by the reciprocity principle.[153] Yang et al.[80] systematically studied the relationship between the resolution of the microsphere lens with different sizes (diameters: 3–21 μm) and the focal width of the nanojet obtained by FEM simulation. The resolution of the microsphere lens, determined as the width of the PSF (σ), is then related to the width of the nanojet (w) with a fitting function: $\sigma = \frac{w}{2\sqrt{2\ln(2)}}$. The best resolution of $\approx$100 nm ($\approx\lambda/6$) was obtained when the diameter of the microsphere is $\approx$6–7 μm. However, the formation of nanojet could not quantitatively explain the superresolution capability of the microsphere lens because it is challenging to anticipate how the high-spatial-frequency components are superposed during the imaging process.

Near-Field-Modified Geometric Optics Explanation: The magnification effect of the microsphere lens can be explained by the geometric optics theory with modifications considering the near-field impact, which has been reported in many works.[79,86,88,89,113] The magnification factor of a microsphere with tens of micrometer diameter is described by geometric optics as:[89] $\text{Mag} = f/(f - r - d)$, $n_r = \frac{n_s}{n_b}$, where $f = d/(\sin\{2\sin^{-1}(\frac{d}{r}) - 2\sin^{-1}[(n_b/n_s)(d/r)]\})$, n_s and n_b are the refractive indices of the spherical lens and background medium, respectively; r is the radius of the spherical lens, d is the distance between the object and the spherical lens surface, f is the focal length of the microsphere from the sphere center. Considering the near field effect, simulation shows a new focal length f and a fitting factor k give rise to a modified magnification factor:[79,113] $\text{Mag} = fk/(f - r - d)$. For the BaTiO$_3$ microsphere lens immersed in water, a factor $k \approx 1.2$ is found by fitting with the experimental results, which corresponds well with the experimental results obtained with different microsphere sizes.[79] The

magnification factor only denotes the enlargement of the sample's image. It does not equal to resolution enhancement, which is an appropriate parameter to quantize the superresolution ability of different setups. Recent work demonstrates a theory exploiting complex Snell's law[146] to explain the process of converting evanescent waves into propagating waves in microsphere lens superresolution imaging. The SF compression factor can be expressed by $M = \frac{\sqrt{k_x^2 + k_y^2}}{n_b k_0}$, where $\sqrt{k_x^2 + k_y^2}$ is the lateral wavevector of evanescent waves and $n_b k_0$ is the maximal lateral wavevector of propagating waves in the background medium.

Although this theory could explain the superresolution ability of the microsphere lens to some extent, it is still difficult to acquire the compression factor without experiments.

Diffractive Optics Explanation: To fully understand the microsphere lens imaging process, images of point emitters at the vicinity of the microsphere can be simulated by solving the Maxwell equations. Previously, the problem was solved using full-wave simulation methods[154] or expansions methods.[144] Recently, Maslov and Astratov compared the focusing and imaging ability of the microsphere lens by using the exact numerical solution of Maxwell equations.[155–158] In their 2D model, the point source emitter put just outside the microsphere lens was used to calculate the impulse response of the system (also termed as the PSF). In this result, the resolution $w/(M\lambda)$ is around 0.42–0.45 and is comparable for small $D/\lambda = 3.5$ and larger $D/\lambda = 6.85$, 9.8 particles. Here we mainly analyze the theory from the perspective of the SFM method. The reader can refer to ref [158] for more detailed information. With the immersion background index of $n = 1.3$–1.5(with an index contrast of 1.4), the diffractive optics theory successfully explains the resolution down to $\lambda/5.6$ less than the $\lambda/7$ reported in other works.[86,121] The small mismatch arises from the fact that experimental conditions are complex processes, which include some physical mechanism that might not be accounted for in this theory, such as the illumination condition (the microsphere lens may focus the illumination into a localized light spot).

3.2.2. Experimental Discoveries of Superresolution Microsphere Lens

The most frequently used microsphere microscopy configuration is the so-called contact mode by merely putting a microsphere lens on top of nanoscale samples and observing from the top using incoherent sources illumination from a conventional microscope.[80,88,114,121]

In 2011, Wang et al.[88] reported a 50 nm resolution optical nanoscope that uses ordinary glass microspheres ($n = 1.46$, 2 μm < diameter <9 μm) to overcome the white-light diffraction limit, attaining a magnification of $\times$4.17 (Figure 4e, gratings) and $\times$8 (Figure 4f, gold-coated fishnet AAO sample) when imaging different samples. The resolution of 50 nm is 4–8 times enhancement compared with that only uses objective lens (NA = 0.9) in visible wavelength (400 to 700 nm), which corresponds to the resolution from 222 to 389 nm.[88] They attribute the outsized magnification factor to the near-field interaction of the sphere with the sample and proposed a fitting formula based on maximal field enhancement: $M \approx (I_{max}/I_0)^{\beta}$, where I_{max}/I_0 is the field enhancement, and β is the fitting exponential parameter. The increase

of the imaging magnification and sharpness for nanostructures samples, as in the AAO case, originates from the plasmonic field enhancement effect.[89] They concluded that the superresolution strength maximized at $n = 1.8$. However, later it was demonstrated microspheres with a higher refractive index ($n \approx 1.9$–2.1) could also be applied in superresolution imaging by totally immersing them in the liquids.[112] They used barium titanate glass (BTG) microspheres for imaging arrays of gold nanoparticle dimers and discerned the minimum feature sizes of $\approx\lambda/7$. The proposal of a high-index liquid-immersed microsphere lens made possible the inspiring application of this technique for imaging biomedical and chemical samples.

Although the first demonstration of the microsphere lens has attracted considerable scientific interests, the lack of control in the microsphere position makes it difficult for practical application. Besides, the sub-100 nm penetration depth Z_m of the evanescent field limits the FOV, as shown in the white dash rectangular of Figure 4b. To obtain a large FOV, self-assembled particle arrays can be used to stitch neighboring unit images. Moreover, a large FOV is also possible when incorporating precise position control of the microsphere for large-area scanning.[78,79,86,87]

Recently, it was demonstrated the high refractive-index microsphere lens could be embedded in the transparent solidified film (such as PMMA and PDMS) for superresolution imaging, which opens a way of scanning microsphere lens imaging by integrating the system with a conventional objective lens.[85,86,91] Compared with air- or liquid-immersed configurations, this amelioration brings in better image quality and robustness to environmental change.[94,145] Another scanning method is integrating microsphere lens with an atomic force microscope (AFM) technique for scanning imaging with a height control of the microsphere above the sample. In 2016 Wang et al.[79] tactfully used a microsphere mounted on an AFM cantilever and achieved superresolution imaging of blue-ray disk surface with a FOV of $\approx 96 \times 96 \ \mu m^2$ in 3 min. The scanning superlens microscopy (SSUM) collects larger FOV in a single collection, providing ≈ 200 times acquisition efficiency compared with ordinary AFM. Then, the scanning process can be realized by moving the sample precisely along the predesigned path. Other interesting scanning methods also include: attaching microsphere to the glass micropipette,[96] using optical tweezers[159] or chemical reaction forces[78] to drive the microsphere lens.

Several works have been reported on increasing the contrast and resolution of microsphere microscopy. One exemplary effort to enhance the imaging contrast is to immerse the microspheres in liquid partially.[92,94,114] In 2014, Yan et al.[92] demonstrated a microsphere-coupled scanning laser confocal microscope (mSLCM), which can discern the gold nanodots with a minimum distance of 25 nm ($\lambda/16.3$) under 408 nm wavelength illumination using fused silica and polystyrene microspheres. The resolution was quantified to be $\approx\lambda/7$ using the more rigorous PSF convolution method.[155] The combination of microsphere microscopy with confocal scanning technique boosted the resolution of mSLCM by a factor of $\approx \sqrt{2}$ comparing with the direct imaging setup.[6,145] Although possessing high imaging resolution, near-field interactions of particle and substrate under a coherent laser illumination will cause multiple ring-shaped

patterns reducing the image quality collected by mSLCM. However, precalculation and erasing the rings from the final image is possible using advanced image processing algorithms.

Recently, it is also found that the natural biomaterials, which can be easily fabricated, could be used as a superlens. The study demonstrated that spider silks spun from the Nephila spider can resolve 100 nm ($\approx\lambda/6$) features under a white-light illuminated microscope.[82] Besides, the living cells with spherical geometry were proved applicable in the superresolution imaging, forming the so-called "bio-magnifier" (Figure 4g).[116] The relatively small refractive index contrast and weak focusing ability could be improved by immersing the cell in water and using a mirror reflection configuration. Cells (such as yeast cells) with smooth surfaces and spherical shapes were chosen to minimize the imaging aberration. The bio-magnifiers have the best magnification factor of 4 and show a resolving ability of 100 nm (sample: nanogap) under white light illumination.

In contrast to biological materials, metamaterial solid immersion lenses (mSIL) were assembled by spherical dielectric nanoparticles using the nanosolid-fluid assembly method. Exploiting 15 nm TiO_2 (refractive index $n = 2.55$) as building blocks, Fan et al.[81] fabricated TiO_2 mSIL with widths of 10–20 μm and demonstrated the assembled 3D all-dielectric mSIL possesses the ability to discern the gold nanodots with the edge-to-edge distance of 45 nm ($\approx\lambda/12$) under white light illumination. The mechanism is a little different from that obtained by a single microsphere lens. For the tightly stacked nanoscale particles (15 nm), the near-field coupling between neighboring particles can effectively transform the propagating wave into patterned evanescent spots for illumination (with a FWHM of ≈ 8 nm) and convert samples' evanescent information into propagating waves. Theoretically, the resolution can be further enhanced by using nanoparticles with smaller size or higher refractive index. The magnification factor varies from 1.8 to 5.3, influenced by the shape (height-to-width ratio) of the mSIL. Similar works have been reported using other materials like ZrO_2 ($n = 2.2$) to replace TiO_2 mixing with polymers, obtaining a resolution of 50 nm under white light illumination.[83]

At last, we conclude from the experimental data and list factors that influence the imaging property of the microsphere lens: 1) Refractive index of the microsphere lens and surrounding medium: Optimal index contrast for virtual imaging is within 1.3–1.7 range, but higher background index can facilitate higher resolution. 2) Refractive index of the sample and substrates: The optical properties of the sample can play a significant role, as well. These include a possibility of excitation of LPs in nanostructured metals as well as SPPs in semiconductor and dielectric structures.[88,160–162] It was also shown that substrates play an important role in imaging magnification and resolution. Theoretical research shows the imaging resolution and the magnification factor are both relative to the refractive index of the substrate.[154] 3) Types of illumination: The excitation of Mie resonances in microspheres and the use of oblique or coherent illumination can favor higher resolution.[79] Besides, confocal illumination can provide a better signal-to-noise ratio compared to wide-field illumination.

**ADVANCED
SCIENCE NEWS**

www.advancedsciencenews.com

LASER
& PHOTONICS
REVIEWS

www.lpr-journal.org
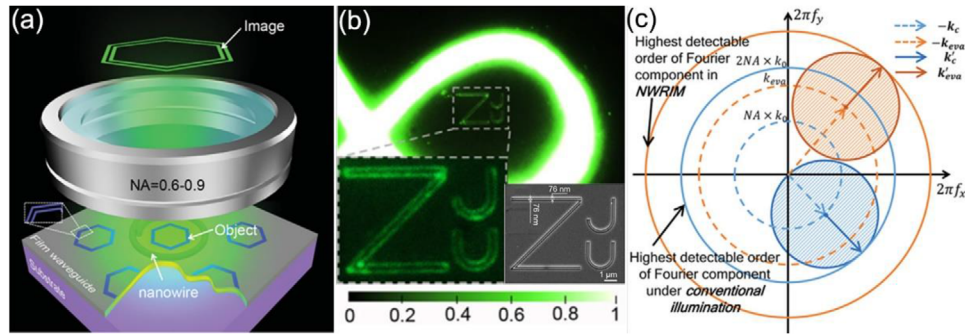
Figure 5. Evanescent wave illumination SFS microscopy. a) Schematic of the configuration and imaging process. b) Evanescent wave illumination SFS images (bottom left) and SEM (bottom right) of an arbitrary ZJU pattern on an Al_2O_3 film. NA = 0.85. c) The underlying mechanism of the evanescent wave illumination SFS method represented in the spatial frequency space. The blue and yellow solid circles in (c) indicate the optical transfer function (OTF) of the conventional microscope system and that of the evanescent wave illumination SFS microscopy. Reproduced with permission.[51] Copyright 2017, American Physical Society.

4. Superresolution Imaging Based on SFS Methods

The employment of evanescent wave's illumination allows the superresolution imaging based on SFS method. To date, a variety of approaches utilizing specially designed substrates to generate evanescent waves for illumination and shift undetectable spatial-frequency signal into the passband of conventional microscope have been proposed.[43,45,51,52,55,119,163–167] Evanescent waves illumination SFS microscopy can be easily constructed by using on-chip techniques and have excellent potential for practical applications.

4.1. SFS with Evanescent Waves Generated by High-Refractive-Index Dielectric Materials

The typical implementation of the SFS method is FPM.[47,49,168] But, to achieve superresolution microscopy, the introduction of evanescent waves becomes the key.[169,170] Evanescent fields occupy the near-field region of dielectric waveguides due to the imaginary transverse wavevector.[171] The magnitude of the in-plane wavevector can be tuned by the waveguide geometry and can thus provide the spatial frequency required to break the diffraction limit for SFS-based new microscopy techniques. Evanescent waves are also used in total internal reflection fluorescence (TIRF) microscopy for enhanced vertical resolution[172–175] and have found full applications in other areas including, coupling devices,[176] sensors,[177–180] and optical tweezers.[181–183] In Section 4.1, we will discuss the SFS superresolution microscopy, which is divided into label-free and labeled methods.

4.1.1. Evanescent Fields Illuminated SFS Label-Free Microscopy

In 2013, Hao et al.[118] utilized evanescent fields along a microoptical fiber as a near-field illumination source and achieved superresolution imaging. The laser guiding microfiber was precisely positioned on the sample surface using a piezoelectric positioning stage. It provided a spatial frequency shift proportional to the effective refractive index of the guided mode. Based on the SFS effect, a slot pair structure of 225 nm central width was successfully resolved under 600 nm wavelength light illumination using

a 0.8 NA objective (0.61 λ/NA = 457 nm). However, the 1D geometry limits the practical 2D imaging due to the difficulty in microfiber positioning.

In 2017, Liu et al.[51] proposed an on-chip evanescent illumination design for label-free 2D subdiffraction-limited imaging with a large FOV. This nanowire (NW) ring illumination microscopy (NWRIM) configuration, enables omnidirectional evanescent wave illumination and is compatible with standard microscopes for efficient superresolution imaging.

Figure 5a shows the schematic of the NWRIM, in which a CdS NW serves as the local light source.[184–186] When the NW is pumped by a 405 nm continuous-wave laser, the excited fluorescent light (center wavelength of ≈520 nm) could efficiently couple into the 200 nm thick TiO_2 film waveguide beneath the NW and illuminate the samples on the waveguide. Thus, scattered light can be collected by a far-field objective, contributing subdiffraction-limited spatial information to the final image. As shown in Figure 5b, the system successively resolved predefined line patterns with 152 nm center-to-center distance slots using a 0.85 NA objective (0.61 λ/NA = 373 nm). Figure 5c shows the detectable spatial frequency components in NWRIM and conventional microscopy, respectively. For conventional microscopy, the wavevector of illumination and detection are both confined by the NA of the objective. Consequently, the detectable Fourier components in far-field are limited to a circle with a radius of 2 NA × k_0. While in NWRIM with an illumination wavevector of k_s, the highest detectable Fourier components are expanded to k_s + NA × k_0, where the illumination wavevector is expressed as

$$k_s = k_0 \times N_{eff} \tag{7}$$

Here N_{eff} is the effective refractive index of the evanescent illumination waves, which could be larger than the NA of the objective lens if a high-refractive-index waveguide is adopted, so that a higher resolution can be achieved correspondingly. They have also employed an Al_2O_3–SiO_2 double-layer waveguide further to extend the propagation length of the evanescent wave and thus the FOV. Later, by optimizing the fabrication process of both the TiO_2 waveguide and the CdS nanowire, they realized an NWRIM with ≈6000 μm^2 FOV and 122 nm center-to-center resolving ability.[119] However, frequency-aliasing is inevitable in

**ADVANCED
SCIENCE NEWS**
www.advancedsciencenews.com

LASER
& PHOTONICS
REVIEWS

www.lpr-journal.org

the nanowire-ring illumination arrangement due to the lack of control on the illuminating directions. The same group[100] reported an upgraded set up in 2019, by using a polygonal-geometry waveguide chip to reduce the frequency aliasing problem. A fluorescent polymer film beneath the TiO_2 waveguide illuminates the sample with evanescent waves traveling along 16 precisely controlled directions. A 2D distortion-less image over $\approx$200 μm^2 FOVs can be reconstructed due to the combination of oblique illumination and multi-wavelengths evanescent wave illumination, which ensures wide coverage of the SF space. In the future, the evanescent wave illumination source could be integrated into the waveguide platform. Recently, a simulation[187] and the initial experiment[188] using Si_3N_4 waveguide have been demonstrated. The fabrication of waveguides is compatible with semiconductor manufacture technologies, which makes the device suitable for practical applications in biological, medical imaging, and diagnostic kits.

4.1.2. Evanescent Fields Illuminated SFS Labeled Microscopy

Among the existing optical superresolution methodologies, the SIM method [109,165,189–191] is one of the most commonly implemented optical superresolution techniques for studying the dynamic biological process at high speed, based on its widefield implement. In SIM, the sample is illuminated with spatially structured excitation light to visualize normally inaccessible high-resolution information in the form of moiré fringes. Theoretically, structured light can be applied into both incoherent imaging (such as fluorescent samples) [163] and coherent imaging (such as scattering samples)[192,193] Here, we mainly discuss the incoherent SIM.

Usually, a sample is illuminated with a sinusoidal light pattern formed by interference expressed as

$$i(x) = i_0 \left[1 + m\cos\left(2\pi k_s x + \varphi\right) \right] \tag{8}$$

where i_0 is the initial intensity, m is the pattern modulation depth, k_s is the spatial frequency of the interference pattern, and φ is the phase constant.

If we think of the imaging process in SF space, the Fourier transform of the final image can be expressed as

$$
\begin{aligned}
F_{\text{fs}}(k) &= [F_o(k) \otimes I(k)] \cdot \text{OTF}(k) \\
&= I_0 \left[F_o(k) + \frac{m}{2} e^{i\varphi} F_o\left(k - k_s\right) \right. \\
&\quad \left. + \frac{m}{2} e^{-i\varphi} F_o\left(k + k_s\right) \right] \cdot \text{OTF}(k)
\end{aligned}
\tag{9}
$$

where $I(k)$ is the Fourier transform of illumination patterns $i(x)$. $F_o(k)$, $F_{\text{fs}}(k)$ are the Fourier spectra of the fluorescence distribution of the sample and the detected image. Thus, the detected spatial spectrum is the superposition of the low-spatial-frequency and two high-spatial-frequency parts of the object. In SF space, the only detectable information resides within a circular region of radius k_c (i.e., 2 NA/λ) around the origin (**Figure 6**). Structured illumination does not alter the observable region physically; instead, it shifts information into the region inward
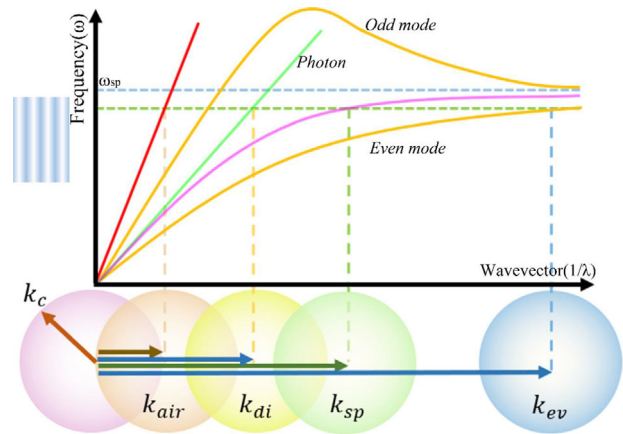
Figure 6. Concept of resolution enhancement by structured illumination. Resolution improvement representation in SF space of SIM, evanescent fields illuminated SIM, and PSIM. Typical dispersion curves of SPPs on a thick-metal-film/dielectric interface (pink curve) and a dielectric/thin-metal-film/dielectric interface (orange curve). The SPP of dielectric/thin-metal-film/dielectric interface splits into the odd mode and even mode when the thickness of the metal decreases to around 50 nm. The pink circle corresponds to the spatial information within the passband of conventional microscopy with k_c representing its cutoff wavevector. The maximum resolution in conventional SIM, as defined by the sum of the cutoff frequency k_c and the spatial-frequency shift k_{air} is approximately twice that of wide-field imaging (The red line represents the dispersion curve of photons in the air.) The evanescent fields illuminated SIM, either TIRF-SIM or cSIM, has a spatial-frequency shift defined by the k_{di}, exceeding that of conventional SIM (The green line represents the dispersion curve of photons in dielectric materials). The wavevector of SPPs is nonlinear with the photon energy. Thus, it is possible to recover information from an area more than twice the size of the normally observable region using PSIM. k_{air}, k_{di}, k_{sp}, k_{ev} represent the spatial-frequency shift obtained in air, dielectric material, single interface SPPs and the even-mode SPPs. ω_{sp} is the surface plasmon frequency.

and thereby makes that information observable. In the reconstruction process, to unmix three spatial frequency components: $F_o(k) \cdot \text{OTF}(k)$, $F_o(k - k_s) \cdot \text{OTF}(k)$, $F_o(k + k_s) \cdot \text{OTF}(k)$, at least three changes in the phase φ of the illumination pattern are required. Also, multiple illumination orientations are favored for full coverage of the 2D SF domain of the planar sample. Detailed reconstruction algorisms can be found in other referenced papers.[194–198]

Here, the SFS effect in SIM is essentially induced by the convolution between the illumination pattern $I(k)$ and the spatial spectrum of the sample $F_o(k)$. The spatial frequency k_s in the illumination pattern determines the highest obtainable SF: $k_{\text{SIM}} = k_c + k_s$. Thus, the innovations on illumination method led to many variants based on SIM with higher resolution, such as SSIM,[44] NL-SIM,[46] PSIM,[52,103] LPSIM,[106,107,159,199,200] and cSIM.[102] The theory also applies to any illumination patterns with high spatial frequencies, such as confocal microscopy and the related spot scanning SIM, which exploit a diffraction-limited excitation focus (or multi-foci) to scan the sample. The excitation focus contains all spatial frequencies up to the cutoff frequency of the condenser objective, enabling a doubled resolution. Some examples of spot scanning SIM include ISM,[201] OPRA,[202] MSIM,[203] and instant SIM.[56] **Table 2** summaries some SIM-based techniques

Table 2. Comparison of various SIM methods.

Methods	Resolution	Objective lens used	Excitation wavelength	Speed per color	Excitation intensity	Ref.
2D-SIM	100 nm (x, y)	100×/1.49	488 nm	0.09 s	5–10 W cm^{-2}	[101,205,304]
High-NA SIM	84 nm (x,y)	100×/1.7	488 nm	0.8 s	30–100 W cm^{-2}	[205]
Hessian-SIM	88 nm (x,y)	100×/1.7	488 nm	0.005 s	187 W cm^{-2}	[165]
3D-SIM	120 nm (x, y) 360 nm (z)	60×/1.2	488 nm	5–25 s	≈5 W cm^{-2}	[305,306]
ISM	150 nm (x, y)	60×/1.2	640 nm	25 s	≈1.5 × 10^3 W cm^{-2}	[201]
OPRA	327 nm (x, y)	63×/0.7	488 nm	10 s	–	[202]
MSIM	145 nm (x, y) 400 nm (z)	60×/1.45	488 nm/561 nm	1 s	–	[203]
instant SIM	145 nm (x,y) 356 nm (z)	100×/1.45	488 nm	0.01 s	≈5–50 W cm^{-2}	[56]
SSIM	48.8 nm (x, y)	100×/1.4	532 nm	16 s	1 × 10^7 W cm^{-2}	[44]
NL-SIM	42 nm (x, y)	100×/1.46	488 nm	100 s	1–10 W cm^{-2}	[46]
PSIM	123 nm (x, y)	63×/1.0	532 nm	–	–	[52,103]
LPSIM	50–74 nm (x, y)	60×/1.2 100×/1.65	405 nm/488 nm/532 nm	0.025–1 s	5–150 W cm^{-2}	[106,107,159,199,200]
cSIM	117 nm (x,y)	60×/1.2	660 nm	–	–	[102]
SIQCM	$m+\sqrt{m}$ fold$^{a)}$	–	–	–	–	[307]

a) The parameter m is the quantum correlation order.

proposed further to improve the resolution as well as other parameters.

TIRF-SIM: The TIRF-SIM method is proposed by using a high-NA objective lens to further extend the lateral resolution of the SIM. The spatial-frequency shift becomes $k_s = \frac{2n\sin\theta}{\lambda_{ex}}$, where n is the refractive index of the matching liquid, θ is the incident angle. Compared with conventional SIM, the illumination pattern now becomes the evanescent waves and can further provide very low background noise and the reduced phototoxicity.

The idea of TIRF-SIM is proposed almost as early as the SIM method[101] but not realized until six years later, where a 1.45 NA objective lens was used, and an ≈100 nm lateral resolution was achieved.[204] In recent work, an ultrahigh 1.7 NA objective was used to achieve a lateral resolution of 84 nm, which allows two-color imaging at intensities of only 30 to 100 W cm^{-2} in a total acquisition time of 1.67 s.[205] The authors used this high-NA TIRF-SIM to study the dynamic associations between proteins with 80–100 time points.

For live-cell imaging, the time resolution is critical. The first in vivo images obtained with TIRF-SIM achieved a ≈110 nm (NA = 1.49, λ_{ex} = 488 nm) resolution at frame rates up to 11 Hz for 180 time points. Later, an imaging speed of 7–20 Hz was reported in several works by using the spatial light modulator.[206,207] Recently, "instant SIM," a multi-spot analog SIM with TIRFM implementation, offers a ≈145 nm lateral and 356 nm axial resolution(NA = 1.45, λ_{ex} = 488 nm) and ≈100 Hz frame rate, dramatically improved the time resolution compared with conventionally TIRF-SIM.[56] Another work, Hessian-SIM, uses the continuity of biological structures in the x, y and time axes as a priori knowledge to guide the reconstruction process, which can obtain artifact-minimized SR images with an 88 nm lateral resolution (NA = 1.7, λ_{ex} = 488 nm) and a 188 Hz ultrahigh frame rate.[165]

The penetration depth of TIRF microscopy can be tuned by changing the incident angle θ, providing a 3D superresolution imaging technique. The typical penetration depth of the evanescent wave is from ≈100 to ≈700 nm,[189,208] depending on the refractive index contrast and the chosen incident angle. By combining this exponential decay leveraging method with TIRF-SIM, the multi-angle interference microscopy (MAIM) can provide a sub-100 nm lateral resolution and 40 nm axial resolution over 600 nm depth range.[189]

Chip-Based SIM (cSIM): In conventional SIM and TIRF-SIM, a large FOV and high resolution cannot be simultaneously obtained. Besides, the commercial liquid immersion objective lens has a limited NA of ≈1.7, which restricts the resolution of TIRF-SIM to around 80 nm.[205] The chip-based SIM break this limitation by using a waveguide to generate standing evanescent-wave interference pattern for SIM. The spatial-frequency shift is no longer limited by the objective lens, but rather depending on the effective refractive index of the waveguide (usually larger than 2.0), and a larger FOV can be obtained by choosing a low-NA objective lens. The spatial-frequency shift in cSIM can be expressed as: $k_s = 2n_f\sin\frac{\theta}{2}/\lambda_{ex}$, where λ_{ex} is the excitation wavelength, n_f is the effective refractive index of the guided mode and θ is the angle of interference. The effective refractive index of the guided mode is usually a little less than the refractive index of the waveguide material. By using natural dielectric material with a high refractive index, like Si_3N_4 (n = 2), Ta_2O_5 (n = 2.1), TiO_2 (n = 2.6), SiC (n = 2.6) or even GaP (n = 3.4),[209] the resolution of cSIM can be potentially reduced to ≈50 nm (TiO_2 waveguide, NA = 1.7, λ_{ex} = 405 nm).

Helle et al.[102] reported a cSIM demonstration using Si_3N_4 waveguide (n_f = 1.7). It reported a 1.2 times resolution enhancement compared with TIRF-SIM, corresponding to a lateral

resolution of 117 nm (NA = 1.2, λ_{ex} = 660 nm). To obtain uniform illumination over a large FOV, a single-mode waveguide is adiabatically tapered[210,211] to a wide waveguide (theoretically applies for waveguides with over several mm² areas). By integrating phase modulation (such as on-chip thermo-optical modulation),[102] cSIM may have opened an avenue for high-throughput, large-producible, and miniaturized superresolution imaging.

4.2. SFS with Plasmonic Structures

To further increase the resolution, illumination with higher spatial frequency is needed. High-refractive-index dielectric materials have demonstrated a successful choice to enhance the resolution by generating evanescent waves illumination in SFS microscopy, as aforementioned. Plasmonic material is another excellent candidate to form excitation illumination with a large spatial frequency, i.e., the SPPs and LPs. SPPs and LPs are demonstrated electromagnetic oscillations generated by collective oscillations of electrons in resonance with a light wave at a conductor/dielectric interface.[212,213] Once excited, SPPs and LPs can be confined to a deep subwavelength scale, leading to a remarkable enhancement of the local field and allowing the manipulation of light far below the diffraction limit.[214] They are attractive for wide-ranging applications, including subwavelength imaging,[215–217] sensing,[218–228] subwavelength waveguides,[229–233] plasmonic lithography,[234–236] photovoltaics,[237–240] optical tweezer,[241–246] and optical analog computing.[247–250]

SPPs were employed in superlens experiments for the SFS based superresolution microscopy as early as 2007.[166,167] In the near-field superlens, the large-wavevector evanescent waves of the sample are resonantly enhanced by the plasmonic superlens slab, thereby generating a superresolution image on the other side.[251] To bring the near-field information into the propagating far-field regime, the far-field superlens was designed with a subwavelength grating on top to downshift the spatial spectrum of the sample.[166,167] Plasmonic waves could also be applied in FPM to provide a better resolution.[48] In this work, SPPs are excited by Kretschmann setup using a 1.4 NA objective and a 2D superresolution imaging is realized (sample: grating structure with 240 nm period width) under 640 nm wavelength light illumination (0.61 λ/NA = 279 nm). Recently, methods using patterned surface plasmons to illuminate the samples have been theoretically proposed and experimentally demonstrated, like PSIM[52,103] and LPSIM.[106,199] The principle, as well as detailed experimental implements of PSIM and LPSIM has been discussed in a book edited by Zhaowei Liu.[252] These methods, combined with fluorescent imaging, demonstrate the biocompatibility and will find applications in future research in biomedical study.

4.2.1. PSIM

Sharing a similar mechanism with SIM, PSIM uses surface plasmon interference (SPI)[253] instead of conventional laser interference to illuminate the sample. Generally, PSIM has a better resolution compared with SIM due to the much smaller period

of SPI, which can bring a higher spatial frequency shift in the spatial frequency space. The spatial frequency shift k_s of PSIM is determined by k_{spp}, which can be tuned by the permittivity of metal and the surrounding dielectric at a specific illumination wavelength. For a metal/dielectric interface, the dispersion relationship of SPPs can be described as

$$\left|k_{spp}\right| = \left|k_0\right| \sqrt{\frac{\varepsilon_m \varepsilon_d}{\varepsilon_m + \varepsilon_d}} \tag{10}$$

where $|k_{spp}|$ and $|k_0|$ represent wavevectors of SPPs and free-space light propagating in vacuum, ε_m and ε_d are the permittivity of metal and dielectric. A comparison of the typical dispersion curves of the SPPs and photons in air and dielectric materials, as plotted in Figure 6, shows that k_{spp} is always greater than k_0, and can be extremely large at the surface plasmon resonant frequency ω_{sp}. Thus, this large wavevector of SPPs can provide a more substantial spatial frequency shift and a higher resolution compared with conventional SIM and evanescent fields illuminated SIM. For insulator–metal–insulator (IMI), the coupling of propagating modes on different interfaces will split the dispersion relationship of SPPs into odd modes and even modes as the metal thickness decreases to tens of nanometers.[131,254] It is worth noting that the $|k_{spp}|$ of even modes will increase inversely with the metal thickness, which is advantageous for superresolution imaging applications. Different modes can be excited individually or simultaneously to form large-wavevector interference patterns that can be used in PSIM.

To launch SPPs, the momentum mismatch between excitation photons and plasmons should be compensated. Existing SPP excitation methods include prism coupling, grating coupling, edge/slit coupling, objective coupling, and near-field excitation.[212] Among these methods, grating coupling,[255] edge/slit coupling,[103] and objective coupling excitation[256–258] are mostly used in PSIM configuration for their convenience in implementation and possibility of generating regular SPP interference patterns, which is superior to irregular ones in terms of resolution and signal-to-noise improvement in the imaging.[259]

The implement of PSIM requires illumination patterns to be tuned with multiple directions and multiple phase shifts. Although the coupling structure geometry is fixed, the SPI direction can be tuned by the illumination polarization, since the SPP coupling efficiency for polarization perpendicular to the coupling structure is more significant than that parallel the coupling structure.[260] To realize the multiple phase shifts in the SPI, controlling the optical delay in individual excitation beams,[255] and controlling optical vortices with topological charges for objective coupling[256] are possible solutions. For edge/slit excitation with multiple periods on the order of micrometers, it is more practical to adjust the angle of incident light to introduce a phase difference $\varphi(\theta)$ between two adjacent edges/slits. This angle variance could translate to a phase difference in the excited SPP waves and thus lateral shift of the interference patterns.

Metal/Dielectric Multilayer Meta-Substrate PSIM: The substrate of PSIM is mainly composed of metal/dielectric multilayer films. In 2012, Wang et al.[255] first experimentally demonstrated the superresolution imaging of nanoparticles using plasmonic standing waves. A 2D PSF FWHM of 172 nm was demonstrated with a fluorescence centered at 645 nm under a 1.42 NA objective

**ADVANCED
SCIENCE NEWS**

www.advancedsciencenews.com

LASER
& PHOTONICS
REVIEWS

www.lpr-journal.org
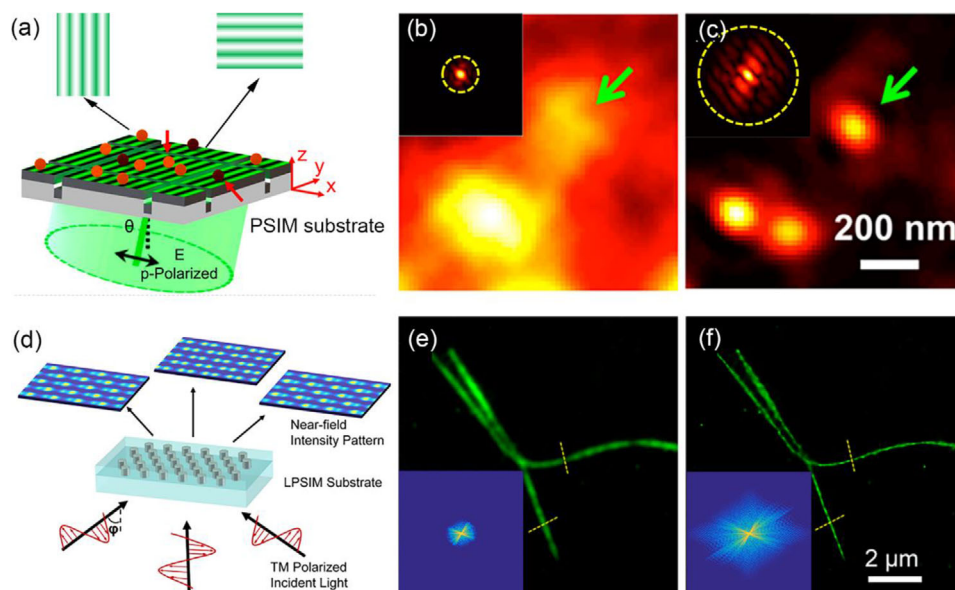
Figure 7. Demonstration of resolution improvement in PSIM and LPSIM. a) Schematic of the PSIM. Green patterns on the top of the substrate are near-field intensity patterns on an object plane generated by p-polarized laser beams in two orthogonal directions. b) Conventional fluorescence image. c) Reconstructed PSIM image. Fourier spectra are shown in the top-left corner of (b,c), respectively. The yellow dashed circles in (b,c) indicate the optical transfer function (OTF) of the conventional microscope system and that of the PSIM system. (a–c) Reproduced with permission.[103] Copyright 2014, American Chemical Society. d) Schematic of the LPSIM. Generated near-field intensity patterns on an object plane created by TM-polarized laser beam incident to the 60 nm hexagonal silver disk array on the sapphire substrate at angles of −60°, 0°, and 60°, along one of the three symmetry axes. e) Diffraction-limited image of green microtubules. f) Corresponding LPSIM image of (e) with significantly improved resolution. Fourier spectra are shown in the bottom-left corner of (e,f), respectively. (d–f) Reproduced with permission.[107] Copyright 2018, American Chemical Society.

lens. In 2014, Wei et al.[103] completed another demonstration of PSIM using a silver film with a thickness of 250 nm and periodic slits array spaced by 7.6 µm to launch counter-propagating SPPs. The propagating SPPs form interference patterns and excite the fluorescence beads with diameters of 100 nm distributing randomly on the silver film surface. Six images with different illumination polarization and angles were recorded and spliced in the SF space to form a large Fourier domain. The FWHM of a single 100 nm diameter fluorescent bead decreases from 327 to 123 nm after SFS processing, yielding a ≈2.6-fold resolution improvement (**Figure 7**a–c).

Further efforts have been devoted to improving the resolution of PSIM with more complex substrates, e.g., the metal-dielectric multilayer. Modes in a metal-dielectric multilayer can be represented by the linear combination of individual surface modes. Thus, as the number of metal films increases, the maximum of the modal index will increase accordingly.[261] The usage of metal-dielectric multilayer to launch deep-subwavelength patterns can be applied in photolithography.[262] Similarly, the metal-dielectric multilayers can also be adopted in PSIM for the generation of large wavevector $|k_{spp}|$.

However, the energy transmission rate is limited due to the significant loss of multilayered metal films. To overcome this problem, Yu and co-workers[263] proposed a six-layer structure (with 1 µm² cross-section area) consisting of Ag–Al₂O₃–Ag–SiO₂–Ag–H₂O to decrease the number of metal films. Finite-difference time-domain (FDTD) Simulation and theoretical calculation demonstrated an interference SPP pattern with a period of 84 nm could be generated at the surface of the substrate. The

postprocess includes illumination with different incident angles and polarizations controls. Finally, the image of a 10 nm diameter quantum dot was reconstructed as a spot with FWHM of 41 nm, which translates to a 5.3-fold improvement compared with conventional epifluorescence microscopy. Different from this work, in ref.[264] the symmetrical coupling of two short-range SPP modes in the dielectric film is used and therefore generating SPPs with ultralarge wavevector. The simulation shows the proposed Ag/Al₂O₃/Ag/H₂O multilayer films could have a high resolution of 16 nm when applied in PSIM, which is 13.6 fold compared with conventional epifluorescent microscopy. The multilayer structure also has an excellent tunability of SPPs by varying the thickness and permittivity of dielectrics.

Graphene-Assisted PSIM: Graphene has been widely investigated for its several unique properties, such as ultrahigh carrier mobility and excellent tunability in conductivity.[265–272] Similar to noble metals supporting collective free electron oscillations, the electrons in the doped graphene can also respond to the electromagnetic field resonantly leading to graphene plasmons (GPs). Comparing with the metal case, the energy loss of the tightly confined GPs is lower, and the propagation length is about a few dozens of wavelengths of the excited mode. Most importantly, the propagation length and the effective refractive index can be dynamically tuned by adjustment of the chemical potential of graphene through applying temperature field,[273] magnetic field,[274] or electrical field.[270] Thanks to these inherent properties, researches on GPs have made remarkable progress[275,276] and found comprehensive applications in transformation optics,[277,278] nanoimaging,[105,279–281] and

tunable metamaterials.[273,282,283] Besides, the developments on upconversion fluorescent nanoparticles, that converse near-infrared (NIR) light to visible wavelengths,[284,285] have made it more easier to facilitate the visible superresolution imaging using GPs in the NIR range. Graphene can be combined with designed substrates to realize ultrahigh-resolution PSIM.

For the graphene layer, the surface conductivity σ_g can be calculated

$$\sigma_g = \frac{ie^2 k_B T}{\pi \hbar^2 (\omega + i/\tau)} \left(\frac{\mu_c}{k_B T} + 2\ln\left(e^{-\frac{\mu_c}{k_B T}} + 1 \right) \right)$$
$$+ \frac{ie^2}{4\pi\hbar} \ln \left| \frac{2\mu_c - \hbar(\omega + i/\tau)}{2\mu_c + \hbar(\omega + i/\tau)} \right| \tag{11}$$

where e represents electron charge, k_B is the Boltzmann constant, T is the Kelvin temperature, $\hbar$ is the reduced Planck constant, ω is the radian frequency, μ_c is the chemical potential, and τ is the electron–phonon relaxation time, respectively. The relative permittivity ϵ_g can be represented as

$$\epsilon_g = 1 + i\frac{\sigma_g}{\epsilon_0 \omega \Delta} \tag{12}$$

where ϵ_0 is the permittivity of vacuum, and Δ denotes the graphene thickness. From Equations (11) and (12), the permittivity of graphene depends on the chemical potential, which can be externally tuned by the bias voltage, thus leads to wavevector tunable GPs.

The graphene-assisted PSIM was first proposed by Zubairy and co-workers[105] In their scheme, GPs were launched by the grating on a dielectric-monolayer graphene-dielectric substrate and a wavevector of $45.7k_0$ was obtained. By optimizing the parameters like the Fermi energy, wavelength of the incident light, and permittivity of the dielectrics, they obtained a 10 nm resolution compared with conventional microscopy.

To further increase the resolution and make it suitable for practical application, another scheme termed as hybrid graphene on metasurface structure (GMS) was proposed.[280] The physical mechanism of GMS is based on localized surface plasmon enhancement and GPs. The GMS structure consists of a single layer of graphene deposited on a $SiO_2/Ag/SiO_2$ multilayer. The 10 nm thick silver film enables a highly localized SPP as the excitation source to GPs lying above. FDTD simulation finds that standing wave GPs with a period of 11 nm can be achieved on graphene for 980 nm wavelength excitation light, and the resolution could reach 6 nm theoretically.

4.2.2. LPSIM

Different from PSIM using propagating SPPs, the LP-SIM uses patterned LPs to illuminate the sample (Figure 7d).[106,107,159,199,200] The illumination patterns are generated by an array of localized plasmon antenna fabricated by electron-beam lithography. Different from SIM or PSIM, whose spatial frequency shift is limited by the free-space or propagating SPP dispersion relations, the period of the structured illumination patterns in LPSIM is only limited by the antenna size geometry thus an arbitrary spatial frequency shift in the Fourier space

could be obtained. Suppose the pitch of the antenna array is p, then the spatial frequency shift k_s can be described as: $k_s = 2\pi/p$.

In 2017, Ponsetto et al.[106] first experimentally confirmed the superresolution ability of LPSIM. The chip is silver nanodisks hexagonally distributed on silica or sapphire substrates. A thin protective layer covered on the silver nanodisks was used to protect the silver from oxidation and separate the silver from the biological samples while the thickness should be small enough to keep the sample in the range of the evanescent plasmonic field. The size and pitch of nanodisks were optimized by simulation. In the experiment, the antenna has a diameter of 60 nm and a pitch of 150 nm. They used this chip to image the fluorescent polystyrene beads (emission wavelength of 500 nm) and achieved a resolution of 74 nm ($\lambda/(5.6 \text{ NA})$). The collected images are far-field fluorescent emission modulated by the localized plasmon generated near-field patterns. To reconstruct the final image, the near-field illuminating patterns should be varied by changing the incident angle. Also, to excite the LPs in the desired direction, the polarization of the incident light should be controlled correspondingly. In 2018, Bezryadina et al.[107] demonstrated a wide-field LPSIM with 50 nm ($\lambda/(6 \text{ NA})$) spatial resolution at video rate speed (30–40 Hz) with comparatively low light intensity (100–150 W cm^{-2}). The 60 nm diameter silver disks with 125 nm pitches were used to achieve the best resolution. The microtubules stained with green fluorescence were imaged in transmission mode with a 100×1.65 NA high-index oil immersion objective, demonstrating the compatibility with live-cell imaging (Figure 7e,f). To further improve the resolution, the LP-SIM could be combined with the spatial frequency compression method. Bezryadina et al.[159] employed optical tweezers to control the microsphere lens on top of the LPSIM substrate with fluorescent objects and obtained a resolution of 57 nm ($\lambda/10$) with a low NA objective lens.

The LPSIM can provide a large shift in the SF space by using nanoantenna arrays with further decreasing the pitch. However, when the pitch is smaller than $\frac{\lambda}{2 \text{ NA}}$, a missing gap will appear in the SF space, which leads to distortion in the final reconstructed image. Recently, it is demonstrated the blind-SIM algorithm is superior to the standard SIM algorithm in the case of information missing in SF space;[200] however, an oversampling should be sacrificed. The blind-SIM algorithm reconstructs the super-resolution image in the real space using a cost-minimization approach. With more information provided, the resolution of the reconstructed image will be better. Nevertheless, it is still hard to achieve the theoretical resolution beyond $\lambda/(6 \text{ NA})$. In the experiment, they used 27 subimages in six directions to obtain an imaging resolution of 81 nm ($\lambda/(5.8 \text{ NA})$), while the theoretical resolution is 52 nm using an array pith of 135 nm with a collecting objective lens of 1.2 NA. Further, the missing spatial frequency could also be filled by designing quasi-periodic structures, each excited by a different illumination wavelength.

Compared with PSIM, the spatial frequency shift of LPSIM is independent of the wavelength and permittivity character. However, to improve the SNR and the imaging speed, the wavelength and permittivity should be carefully chosen to ensure the resonant plasmonic enhancement. The illumination of LPSIM is a paralleled point scanning using nanoantenna fields, separating the illumination and detection lens; thus, a large spatial frequency shift imaging with a large FOV could be obtained at

**ADVANCED
SCIENCE NEWS**

www.advancedsciencenews.com

LASER
& PHOTONICS
REVIEWS

www.lpr-journal.org
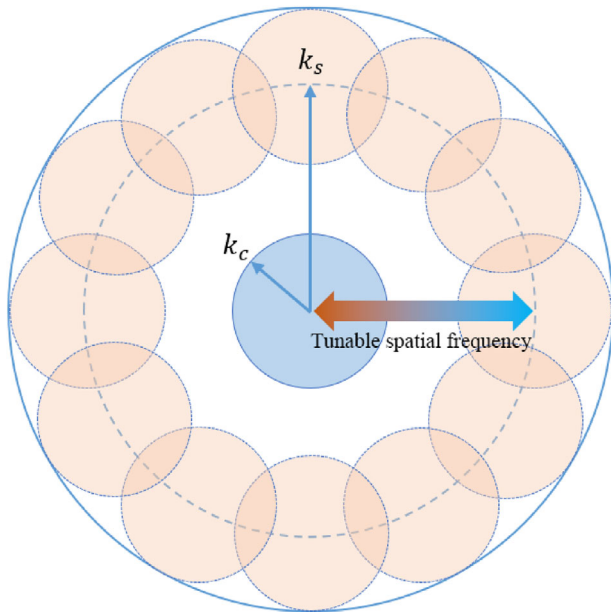
Figure 8. SFS method with tunable spatial frequency. To reconstruct a superresolution image with high fidelity, tuning wavevector in an extensive range is necessary.

high speeds. The limit of the LPSIM is the large-scale fabrication, the imperfection of which will bring wrong sampling and generate a distorted image. Similar to other near-field illumination superresolution imaging methods, LPSIM can only detect the sample structures with a thickness within the depth of the evanescent waves. From another point of view, the sectioning ability will bring a better imaging contrast by cutting off the out-of-focus noise.

4.3. SFS with Tunable Spatial Frequency

For SFS methods, the existing problem remains in the acquirement of evanescent wave illumination with large and tunable wavevectors. Like in other superresolution imaging methods that operate in the SF domain, the spatial frequency stitching is a critical step to achieve the final image for SFS methods. A reconstruction image with higher resolution and fidelity requires multiple spatial frequency shifts with an overlap between adjacent shifted domains.[51,197] Thus, a large and continuously tunable wavevector is a necessity (**Figure 8**). The large-wavevector evanescent waves could be provided by a high-refractive-index waveguide or HMMs without wavevector cutoff.[50,138,286,287] Various researches have been done to continuously tune the wavevector. For dielectric waveguides, one direct way is to adapt the wavevector of evanescent waves by varying the wavelength of the incident light. For metal/dielectric substrates, the wavevector of launched SPPs could be dynamically tuned by externally controlling the hyperbolic dispersion. Various approaches, such as optical excitation, electrical gating, and external temperature variation, have been combined with tunable constituent materials to launch wavevector-tunable evanescent waves.[288]

Another scheme is to use specially designed substrate to generate multiple spatial frequencies simultaneously, which is similar

to that in saturated structured illumination (SSIM)[44] and nonlinear structured-illumination microscopy (NL-SIM).[46]

The tunable spatial frequency has not attracted enough attention. In future research, deep and tunable frequency shift will be an essential and useful approach to obtain sub-50 nm wide-field far-field resolution superresolution imaging, which is necessary for nanoscale imaging and analysis in biology and materials.

5. Future Perspectives/Outlook

Just a few years after the first implementation, superresolution techniques are transforming our understanding of optical physics along with the microscopic biology world. Ongoing developments suggest that an impressive diversity of biological and medical questions could be answered using optical nanoscopy. As complementary techniques of existing far-field nanoscopy like STED and STORM, evanescent wave assisted superresolution methods have shown us their power in resolution, imaging speed, and FOV. Compared with conventional imaging methods used for the detection of subwavelength details relying on relatively sophisticated, cumbersome, and expensive microscopy systems, chip-based superresolution methods provide new avenues toward cost-effective and easy-to-use superresolution imaging. Besides, superresolution methods based on large-wavevector electromagnetic evanescent waves put less requirement on special fluorescent dyes and will find wide applications in biology, medicine, and semiconductor industry.

Although we have addressed many benefits gained from these superresolution techniques, it is worth noting that there is still no ideal method to possess all advantages simultaneously. For instance, NWRIM can have a large FOV and fast imaging speed but sacrifices the resolution improvement, while for microsphere nanoscopy, the resolution and the scanning imaging speed are contradictory. Besides, methods based on SFM are typically associated with evanescent waves, requiring near-field interactions with samples, either with an evanescent-wave-generating substrate or a superlens. Therefore, the application of these superresolution methods is highly dependent on the comprehensive understanding of the requirements of the end-user. As nascent technologies, these superresolution methods also face challenges from other techniques and require new technology advancements.

Resolution and imaging quality are the priorities of a superresolution system. For surface-wave based superresolution methods, the key to improving the resolution and image quality is finding new materials with high refractive index and low optical loss. Metamaterials fill in the gaps by providing the ability to generate large-wavevector evanescent waves or collect evanescent waves efficiently. The realization of a theoretical perfect superresolution device is possible with judicious design processes. However, the limit in fabrication accuracy and throughput of current technologies, e.g., electron beam lithography[289] and focused ion beams,[290] should be further enhanced to meet the ever-increasing demand for precision and large-scale fabrication.[291] Another promising direction is the combination with other nanoscopy methods, which is termed as correlative superresolution microscopy.[292,293] Typical ideas of chip-based correlative superresolution microscopy are SSUM (combining microsphere lens with AFM system),[79] mSLCM (combining

**ADVANCED
SCIENCE NEWS**

www.advancedsciencenews.com

**LASER
& PHOTONICS
REVIEWS**

www.lpr-journal.org

microspheres with scanning laser confocal microscope),[92] and chip-based dSTORM.[294] Such combined approaches either provide valuable contextual information or improve imaging performance such as resolution, FOV, or speed. In addition, all these imaging methods could be combined with the recently developed deep-learning approaches to improve the resolution and the imaging quality further.[295–297] Finally, the chip-based superresolution imaging method will give full play to its superiority if combined with integrated technologies. For example, a field-portable superresolution imaging device can be obtained if we can develop a lightweight and compact optomechanical adaptor to make the superresolution chip adapt to the existing camera module of a cell phone.[298] Further, the chip-based superresolution methods could develop into diagnostic tools for use at the point of care (POC) if combined with other sensing or detecting technologies.[299,300]

As the microsphere nanoscopy is now becoming commercially available, it is exhilarating to expect more commercialized superresolution microscopy and their applications in research or industry in the near future.

Acknowledgements

Conflict of Interest

The authors declare no conflict of interest.

Keywords

[1] E. Abbe, *Ark. Mikrosk. Anat.* **1873**, *9*, 413.
[2] H. von Helmholtz, *Ann. Phys.* **1874**, 557.
[3] M. Minsky, *US3013467*, **1961**.
[4] G. J. Brakenhoff, H. T. M. Vandervoort, E. A. Vanspronsen, W. A. M. Linnemans, N. Nanninga, *Nature* **1985**, *317*, 748.
[5] C. J. R. Sheppard, S. B. Mehta, R. Heintzmann, *Opt. Lett.* **2013**, *38*, 2889.
[6] J. Pawley, *Handbook of Biological Confocal Microscopy*, Springer Science & Business Media, New York **2010**.
[7] S. J. Sahl, S. W. Hell, S. Jakobs, *Nat. Rev. Mol. Cell Biol.* **2017**, *18*, 685.
[8] S. W. Hell, J. Wichmann, *Opt. Lett.* **1994**, *19*, 780.
[9] K. I. Willig, B. Harke, R. Medda, S. W. Hell, *Nat. Methods* **2007**, *4*, 915.
[10] T. A. Klar, S. W. Hell, *Opt. Lett.* **1999**, *24*, 954.
[11] K. I. Willig, S. O. Rizzoli, V. Westphal, R. Jahn, S. W. Hell, *Nature* **2006**, *440*, 935.
[12] M. Hofmann, C. Eggeling, S. Jakobs, S. W. Hell, *Proc. Natl. Acad. Sci. USA* **2005**, *102*, 17565.
[13] S. Waeldchen, J. Lehmann, T. Klein, S. van de Linde, M. Sauer, *Sci. Rep.* **2015**, *5*, 15348.
[14] P. P. Laissue, R. A. Alghamdi, P. Tomancak, E. G. Reynaud, H. Shroff, *Nat. Methods* **2017**, *14*, 657.
[15] S. W. Hell, M. Kroug, *Appl. Phys. B: Lasers Opt.* **1995**, *60*, 495.
[16] G. Donnert, J. Keller, R. Medda, M. A. Andrei, S. O. Rizzoli, R. Luehrmann, R. Jahn, C. Eggeling, S. W. Hell, *Proc. Natl. Acad. Sci. USA* **2006**, *103*, 11440.
[17] R. Heintzmann, T. M. Jovin, C. Cremer, *J. Opt. Soc. Am. A* **2002**, *19*, 1599.
[18] J. Enderlein, *Appl. Phys. Lett.* **2005**, *87*, 097105.
[19] M. J. Rust, M. Bates, X. Zhuang, *Nat. Methods* **2006**, *3*, 793.
[20] S. A. Jones, S.-H. Shim, J. He, X. Zhuang, *Nat. Methods* **2011**, *8*, 499.
[21] E. Betzig, G. H. Patterson, R. Sougrat, O. W. Lindwasser, S. Olenych, J. S. Bonifacino, M. W. Davidson, J. Lippincott-Schwartz, H. F. Hess, *Science* **2006**, *313*, 1642.
[22] S. T. Hess, T. P. Girirajan, M. D. Mason, *Biophys. J.* **2006**, *91*, 4258.
[23] B. R. Masters, *Super-Resolution Microscopy Techniques in the Neurosciences*, Humana Press, Totowa, NJ **2015**.
[24] E. Kim, M. D. Baaske, I. Schuldes, P. S. Wilsch, F. Vollmer, *Sci. Adv.* **2017**, *3*, 8.
[25] S. Subramanian, H. Y. Wu, T. Constant, J. Xavier, F. Vollmer, *Adv. Mater.* **2018**, *30*, 1801246.
[26] S. W. Hell, *Science* **2007**, *316*, 1153.
[27] H. Blom, J. Widengren, *Chem. Rev.* **2017**, *117*, 7377.
[28] D. Baddeley, J. Bewersdorf, *Annu. Rev. Biochem.* **2018**, *87*, 965.
[29] Y. M. Sigal, R. B. Zhou, X. W. Zhuang, *Science* **2018**, *361*, 880.
[30] A. von Diezmann, Y. Shechtman, W. E. Moerner, *Chem. Rev.* **2017**, *117*, 7244.
[31] L. Schermelleh, R. Heintzmann, H. Leonhardt, *J. Cell Biol.* **2010**, *190*, 165.
[32] C. G. Galbraith, J. A. Galbraith, *J. Cell Sci.* **2011**, *124*, 1607.
[33] G. Vicidomini, P. Bianchini, A. Diaspro, *Nat. Methods* **2018**, *15*, 173.
[34] E. T. F. Rogers, N. I. Zheludev, *J. Opt.* **2013**, *15*, 094008.
[35] G. Chen, Z.-Q. Wen, C.-W. Qiu, *Light: Sci Appl.* **2019**, *8*, 56.
[36] M. V. Berry, S. Popescu, *J. Phys. A: Math. Gen.* **2006**, *39*, 6965.
[37] F. M. Huang, N. I. Zheludev, *Nano Lett.* **2009**, *9*, 1249.
[38] F. M. Huang, N. Zheludev, Y. Chen, F. Javier Garcia de Abajo, *Appl. Phys. Lett.* **2007**, *90*, 091119.
[39] K. Huang, H. Ye, J. Teng, S. P. Yeo, B. Luk'yanchuk, C. Qiu, *Laser Photonics Rev.* **2014**, *8*, 152.
[40] F. Qin, K. Huang, J. Wu, J. Teng, C. W. Qiu, M. Hong, *Adv. Mater.* **2017**, *29*, 1602721.
[41] E. T. F. Rogers, J. Lindberg, T. Roy, S. Savo, J. E. Chad, M. R. Dennis, N. I. Zheludev, *Nat. Mater.* **2012**, *11*, 432.
[42] K. Huang, F. Qin, H. Liu, H. Ye, C. W. Qiu, M. Hong, B. Luk'yanchuk, J. Teng, *Adv. Mater.* **2018**, *30*, 1704556.
[43] R. Heintzmann, T. M. Jovin, C. Cremer, *J. Opt. Soc. Am. A* **2002**, *19*, 1599.
[44] M. G. Gustafsson, *Proc. Natl. Acad. Sci. USA* **2005**, *102*, 13081.
[45] M. G. L. Gustafsson, L. Shao, P. M. Carlton, C. J. R. Wang, I. N. Golubovskaya, W. Z. Cande, D. A. Agard, J. W. Sedat, *Biophys. J.* **2008**, *94*, 4957.
[46] E. H. Rego, L. Shao, J. J. Macklin, L. Winoto, G. A. Johansson, N. Kamps-Hughes, M. W. Davidson, M. G. Gustafsson, *Proc. Natl. Acad. Sci. USA* **2012**, *109*, E135.
[47] G. Zheng, R. Horstmeyer, C. Yang, *Nat. Photonics* **2013**, *7*, 739.
[48] Q. L. Liu, Y. Fang, R. J. Zhou, P. Xiu, C. F. Kuang, X. Liu, *Opt. Lett.* **2016**, *41*, 5373.
[49] L. Tian, X. Li, K. Ramchandran, L. Waller, *Biomed. Opt. Express* **2014**, *5*, 2376.
[50] D. Lu, Z. Liu, *Nat. Commun.* **2012**, *3*, 1205.

[51] X. W. Liu, C. F. Kuang, X. Hao, C. L. Pang, P. F. Xu, H. F. Li, Y. Liu, C. Yu, Y. K. Xu, D. Nan, W. D. Shen, Y. Fang, L. N. He, X. Liu, Q. Yang, *Phys. Rev. Lett.* **2017**, *118*, 076101.

[52] F. Wei, Z. Liu, *Nano Lett.* **2010**, *10*, 2531.

[53] M. Saxena, G. Eluru, S. S. Gorthi, *Adv. Opt. Photonics* **2015**, *7*, 241.

[54] Y. Wu, H. Shroff, *Nat. Methods* **2018**, *15*, 1011.

[55] D. Dan, M. Lei, B. Yao, W. Wang, M. Winterhalder, A. Zumbusch, Y. Qi, L. Xia, S. Yan, Y. Yang, P. Gao, T. Ye, W. Zhao, *Sci. Rep.* **2013**, *3*, 1116.

[56] A. G. York, P. Chandris, D. D. Nogare, J. Head, P. Wawrzusin, R. S. Fischer, A. Chitnis, H. Shroff, *Nat. Methods* **2013**, *10*, 1122.

[57] Y. Hirano, A. Matsuda, Y. Hiraoka, *Microscopy* **2015**, *64*, 237.

[58] G. Komis, M. Mistrik, O. Šamajová, M. Ovečka, J. Bartek, J. Šamaj, *Nat. Protoc.* **2015**, *10*, 1248.

[59] E. Wegel, A. Gohler, B. C. Lagerholm, A. Wainman, S. Uphoff, R. Kaufmann, I. M. Dobbie, *Sci. Rep.* **2016**, *6*, 27290.

[60] G. T. Di Francia, *Nuovo Cimento* **1952**, *9*, 426.

[61] N. Rotenberg, L. Kuipers, *Nat. Photonics* **2014**, *8*, 919.

[62] J. Kim, K. B. Song, *Micron* **2007**, *38*, 409.

[63] A. Bek, R. Vogelgesang, K. Kern, *Rev. Sci. Instrum.* **2006**, *77*, 043703.

[64] B. Hecht, B. Sick, U. P. Wild, V. Deckert, R. Zenobi, O. J. F. Martin, D. W. Pohl, *J. Chem. Phys.* **2000**, *112*, 7761.

[65] R. C. Dunn, *Chem. Rev.* **1999**, *99*, 2891.

[66] F. Zenhausern, Y. Martin, H. K. Wickramasinghe, *Science* **1995**, *269*, 1083.

[67] X. S. Xie, R. C. Dunn, *Science* **1994**, *265*, 361.

[68] E. Betzig, J. K. Trautman, *Science* **1992**, *257*, 189.

[69] D. W. Pohl, W. Denk, M. Lanz, *Appl. Phys. Lett.* **1984**, *44*, 651.

[70] J. Rho, Z. Ye, Y. Xiong, X. Yin, Z. Liu, H. Choi, G. Bartal, X. Zhang, *Nat. Commun.* **2010**, *1*, 143.

[71] J. Sun, M. I. Shalaev, N. M. Litchinitser, *Nat. Commun.* **2015**, *6*, 7201.

[72] D. Lee, Y. D. Kim, M. Kim, S. So, H.-J. Choi, J. Mun, D. M. Nguyen, T. Badloe, J. G. Ok, K. Kim, H. Lee, J. Rho, *ACS Photonics* **2018**, *5*, 2549.

[73] M. Byun, D. Lee, M. Kim, Y. Kim, K. Kim, J. G. Ok, J. Rho, H. Lee, *Sci. Rep.* **2017**, *7*, 46314.

[74] L. Chen, G. P. Wang, *Opt. Express* **2009**, *17*, 3903.

[75] S. Han, Y. Xiong, D. Genov, Z. Liu, G. Bartal, X. Zhang, *Nano Lett.* **2008**, *8*, 4243.

[76] Z. Liu, H. Lee, Y. Xiong, C. Sun, X. Zhang, *Science* **2007**, *315*, 1686.

[77] Z. Jacob, L. V. Alekseyev, E. Narimanov, *Opt. Express* **2006**, *14*, 8247.

[78] J. Li, W. Liu, T. Li, I. Rozen, J. Zhao, B. Bahari, B. Kante, J. Wang, *Nano Lett.* **2016**, *16*, 6604.

[79] F. Wang, L. Liu, H. Yu, Y. Wen, P. Yu, Z. Liu, Y. Wang, W. J. Li, *Nat. Commun.* **2016**, *7*, 13748.

[80] H. Yang, R. Trouillon, G. Huszka, M. A. Gijs, *Nano Lett.* **2016**, *16*, 4862.

[81] F. Wen, Y. Bing, Z. Wang, L. Wu, *Sci. Adv.* **2016**, *2*, 1600901.

[82] J. N. Monks, B. Yan, N. Hawkins, F. Vollrath, Z. Wang, *Nano Lett.* **2016**, *16*, 5842.

[83] H. Zhu, W. Fan, S. Zhou, M. Chen, L. Wu, *ACS Nano* **2016**, *10*, 9755.

[84] H. Yang, N. Moullan, J. Auwerx, M. A. M. Gijs, *Small* **2014**, *10*, 1712.

[85] B. Yan, Z. Wang, A. L. Parker, Y. K. Lai, P. John Thomas, L. Yue, J. N. Monks, *Appl. Opt.* **2017**, *56*, 3142.

[86] K. W. Allen, N. Farahi, Y. Li, N. I. Limberopoulos, D. E. Walker, A. M. Urbas, V. Liberman, V. N. Astratov, *Ann. Phys.* **2015**, *527*, 513.

[87] G. Huszka, M. A. M. Gijs, *Sci. Rep.* **2018**, *8*, 601.

[88] Z. Wang, W. Guo, L. Li, B. Luk'yanchuk, A. Khan, Z. Liu, Z. Chen, M. Hong, *Nat. Commun.* **2011**, *2*, 218.

[89] L. Li, W. Guo, Y. Yan, S. Lee, T. Wang, *Light: Sci. Appl.* **2013**, *2*, 104.

[90] M. Guo, Y.-H. Ye, J. Hou, B. Du, *Photonics Res.* **2015**, *3*, 339.

[91] A. Darafsheh, C. Guardiola, A. Palovcak, J. C. Finlay, A. Carabe, *Opt. Lett.* **2015**, *40*, 5.

[92] Y. Yan, L. Li, C. Feng, W. Guo, S. Lee, M. Hong, *ACS Nano* **2014**, *8*, 1809.

[93] J. Y. Lee, B. H. Hong, W. Y. Kim, S. K. Min, Y. Kim, M. V. Jouravlev, R. Bose, K. S. Kim, I.-C. Hwang, L. J. Kaufman, C. W. Wong, P. Kim, K. S. Kim, *Nature* **2009**, *460*, 498.

[94] A. Darafsheh, *Opt. Lett.* **2017**, *42*, 735.

[95] A. Darafsheh, N. I. Limberopoulos, J. S. Derov, D. E. Walker, Jr., V. N. Astratov, *Appl. Phys. Lett.* **2014**, *104*, 061117.

[96] L. A. Krivitsky, J. J. Wang, Z. Wang, B. Luk'yanchuk, *Sci. Rep.* **2013**, *3*, 3501.

[97] E. Hecht, *Optics*, Pearson Education, London, UK **2016**.

[98] G. Gay, O. Alloschery, B. V. De Lesegno, C. O'Dwyer, J. Weiner, H. Lezec, *Nat. Phys.* **2006**, *2*, 262.

[99] E. Hutter, J. H. Fendler, *Adv. Mater.* **2004**, *16*, 1685.

[100] C. Pang, J. Li, M. Tang, J. Wang, I. Mela, F. Ströhl, L. Hecker, W. Shen, Q. Liu, X. Liu, Y. Wang, H. Zhang, M. Xu, X. Zhang, X. Liu, Q. Yang, C. F. Kaminski, *Adv. Funct. Mater.* **2019**, *29*, 1900126.

[101] G. E. Cragg, P. T. So, *Opt. Lett.* **2000**, *25*, 46.

[102] Ø. I. Helle, F. T. Dullo, M. Lahrberg, J.-C. Tinguely, O. G. Hellesø, B. S. Ahluwalia, *Nat. Photonics* **2020**, *14*, 431.

[103] F. Wei, D. Lu, H. Shen, W. Wan, J. L. Ponsetto, E. Huang, Z. Liu, *Nano Lett.* **2014**, *14*, 4634.

[104] C. Zhang, L. Du, Z. Xin, G. Si, A. Yang, T. Lei, J. Lin, X. Yuan, *Laser Photonics Rev.* **2018**, *12*, 1800148.

[105] X. Zeng, M. Al-Amri, M. S. Zubairy, *Phys. Rev. B* **2014**, *90*, 235418.

[106] J. L. Ponsetto, A. Bezryadina, F. Wei, K. Onishi, H. Shen, E. Huang, L. Ferrari, Q. Ma, Y. Zou, Z. Liu, *ACS Nano* **2017**, *11*, 5344.

[107] A. Bezryadina, J. Zhao, Y. Xia, X. Zhang, Z. Liu, *ACS Nano* **2018**, *12*, 8248.

[108] B. S. Luk'yanchuk, R. Paniagua-Domínguez, I. Minin, O. Minin, Z. Wang, *Opt. Mater. Express* **2017**, *7*, 1820.

[109] F. Ströhl, C. F. Kaminski, *Optica* **2016**, *3*, 667.

[110] X. Hao, C. F. Kuang, Z. T. Gu, Y. F. Wang, S. A. Li, Y. L. Ku, Y. H. Li, J. H. Ge, X. Liu, *Light: Sci. Appl.* **2013**, *2*, e108.

[111] L. Rayleigh, *London, Edinburgh Dublin Philos. Mag. J. Sci.* **1879**, *8*, 261.

[112] A. Darafsheh, G. F. Walsh, L. Dal Negro, V. N. Astratov, *Appl. Phys. Lett.* **2012**, *101*, 141128.

[113] L.-W. Chen, Y. Zhou, M.-X. Wu, M.-H. Hong, *Opto-Electron. Adv.* **2018**, *1*, 17000101.

[114] X. Hao, C. Kuang, X. Liu, H. Zhang, Y. Li, *Appl. Phys. Lett.* **2011**, *99*, 203102.

[115] S. Lee, L. Li, Y. Ben-Aryeh, Z. Wang, W. Guo, *J. Opt.* **2013**, *15*, 125710.

[116] Y. Li, X. Liu, B. Li, *Light: Sci. Appl.* **2019**, *8*, 61.

[117] X. Hao, C. Kuang, Y. Li, X. Liu, *Opt. Lett.* **2013**, *38*, 2455.

[118] X. Hao, X. Liu, C. Kuang, Y. Li, Y. Ku, H. Zhang, H. Li, L. Tong, *Appl. Phys. Lett.* **2013**, *102*, 013104.

[119] C. Pang, X. Liu, M. Zhuge, X. Liu, M. G. Somekh, Y. Zhao, D. Jin, W. Shen, H. Li, L. Wu, C. Wang, C. Kuang, Q. Yang, *Opt. Lett.* **2017**, *42*, 4569.

[120] K. W. Allen, N. Farahi, Y. Li, N. I. Limberopoulos, D. E. Walker, A. M. Urbas, V. N. Astratov, *NAECON 2014-IEEE National Aerospace and Electronics Conference, Super-Resolution Imaging by Arrays of High-Index Spheres Embedded in Transparent Matrices*, IEEE, Dayton, OH **2014**.

[121] K. W. Allen, N. Farahi, Y. Li, N. I. Limberopoulos, D. E. Walker, Jr., A. M. Urbas, V. N. Astratov, *Opt. Express* **2015**, *23*, 24484.

[122] W. V. Houston, *Phys. Rev.* **1927**, *29*, 478.

[123] S. M. Mansfield, G. S. Kino, *Appl. Phys. Lett.* **1990**, *57*, 2615.

[124] Q. Ma, H. Hu, E. Huang, Z. Liu, *Nanoscale* **2017**, *9*, 18268.

[125] P. Lalanne, P. Chavel, *Laser Photonics Rev.* **2017**, *11*, 1600295.

[126] K. Wu, G. P. Wang, *Sci. Rep.* **2016**, *6*, 38651.

[127] L. Ferrari, C. Wu, D. Lepage, X. Zhang, Z. Liu, *Prog. Quantum Electron.* **2015**, *40*, 1.

[128] T. Li, J. B. Khurgin, *Optica* **2016**, *3*, 1388.

[129] A. Poddubny, I. Iorsh, P. Belov, Y. Kivshar, *Nat. Photonics* **2013**, *7*, 948.

[130] A. A. Orlov, S. V. Zhukovsky, I. V. Iorsh, P. A. Belov, *Photonics Nanostruct.* **2014**, *12*, 213.

[131] X. Luo, *Sci. China: Phys., Mech. Astron.* **2015**, *58*, 594201.

[132] X. Ni, S. Ishii, M. D. Thoreson, V. M. Shalaev, S. Han, S. Lee, A. V. Kildishev, *Opt. Express* **2011**, *19*, 25242.

[133] Y. Ra'Di, V. S. Asadchy, S. A. Tretyakov, *IEEE Trans. Antennas Propag.* **2013**, *61*, 4606.

[134] J. Yao, Z. Liu, Y. Liu, Y. Wang, C. Sun, G. Bartal, A. M. Stacy, X. Zhang, *Science* **2008**, *321*, 930.

[135] C. Guclu, S. Campione, F. Capolino, *Phys. Rev. B* **2012**, *86*, 7.

[136] T. U. Tumkur, L. Gu, J. K. Kitur, E. E. Narimanov, M. A. Noginov, *Appl. Phys. Lett.* **2012**, *100*, 161103.

[137] E. Narimanov, *ACS Photonics* **2016**, *3*, 1090.

[138] Q. Ma, H. Qian, S. Montoya, W. Bao, L. Ferrari, H. Hu, E. Khan, Y. Wang, E. E. Fullerton, E. E. Narimanov, X. Zhang, Z. Liu, *ACS Nano* **2018**, *12*, 11316.

[139] Y. Xiong, Z. Liu, X. Zhang, *Appl. Phys. Lett.* **2009**, *94*, 203108.

[140] J. Sun, N. M. Litchinitser, *ACS Nano* **2018**, *12*, 542.

[141] J. Sun, T. Xu, N. M. Litchinitser, *Nano Lett.* **2016**, *16*, 7905.

[142] V. Astratov, *Label-Free Super-Resolution Microscopy*, Springer, Switzerland **2019**.

[143] J. W. Goodman, *Introduction to Fourier Optics*, W. H. Freeman, New York **2005**.

[144] Y. Duan, G. Barbastathis, B. Zhang, *Opt. Lett.* **2013**, *38*, 2988.

[145] Z. Wang, *Nanoscience* **2016**, *3*, 193.

[146] Y. Ben-Aryeh, *J. Opt. Soc. Am. A* **2016**, *33*, 2284.

[147] R. Malureanu, O. Takayama, E. Shkondin, A. Novitsky, A. V. Lavrinenko, *OSA Continuum* **2020**, *3*, 10.

[148] S. Perrin, H. Li, A. Leong-Hoi, S. Lecler, P. Montgomery, *J. Microsc.* **2019**, *274*, 69.

[149] Z. Chen, A. Taflove, V. Backman, *Opt. Express* **2004**, *12*, 1214.

[150] P. Ferrand, J. Wenger, A. Devilez, M. Pianta, B. Stout, N. Bonod, E. Popov, H. Rigneault, *Opt. Express* **2008**, *16*, 6930.

[151] A. Heifetz, S. C. Kong, A. V. Sahakian, A. Taflove, V. Backman, *J. Comput. Theor. Nanosci.* **2009**, *6*, 1979.

[152] M.-S. Kim, T. Scharf, S. Mühlig, C. Rockstuhl, H. P. Herzig, *Opt. Express* **2011**, *19*, 10206.

[153] M. Mansuripur, *Opt. Photonics News* **1998**, *9*, 53.

[154] V. M. Sundaram, S.-B. Wen, *Appl. Phys. Lett.* **2014**, *105*, 204102.

[155] A. V. Maslov, V. N. Astratov, *Phys. Rev. Appl.* **2019**, *11*, 064004.

[156] A. V. Maslov, V. N. Astratov, *Appl. Phys. Lett.* **2017**, *110*, 261107.

[157] A. V. Maslov, V. N. Astratov, *Appl. Phys. Lett.* **2016**, *108*, 051104.

[158] A. V. Maslov, V. N. Astratov, *ASTRATOV V. Label-Free Super-Resolution Microscopy*, Springer International Publishing, Cham **2019**, 407.

[159] A. Bezryadina, J. X. Li, J. X. Zhao, A. Kothambawala, J. Ponsetto, E. Huang, J. Wang, Z. W. Liu, *Nanoscale* **2017**, *9*, 14907.

[160] V. N. Astratov, F. Abolmaali, A. Brettin, G. W. Bidney, B. Jin, N. I. Limberopoulos, D. E. Walker, H. Li, A. V. Maslov, presented at *2019 21st Int. Conf. on Transparent Optical Networks (ICTON), Resolution Enhancement in Microspherical Nanoscopy by Coupling of Emission to Plasmonics Metasurfaces*, Angers, France, July **2019**.

[161] A. Brettin, F. Abolmaali, K. F. Blanchette, C. L. McGinnis, Y. E. Nesmelov, N. I. Limberopoulos, D. E. Walker, I. Anisimov, A. M. Urbas, L. Poffo, A. V. Maslov, V. N. Astratov, *Appl. Phys. Lett.* **2019**, *114*, 131101.

[162] S. Yang, Y. Cao, Q. Shi, X. Wang, T. Chen, J. Wang, Y.-H. Ye, *J. Phys. Chem. C* **2019**, *123*, 28353.

[163] M. G. Gustafsson, *J. Microsc.* **2000**, *198*, 82.

[164] L. M. Hirvonen, K. Wicker, O. Mandula, R. Heintzmann, *Eur. Biophys. J. Biophys. Lett.* **2009**, *38*, 807.

[165] X. Huang, J. Fan, L. Li, H. Liu, R. Wu, Y. Wu, L. Wei, H. Mao, A. Lal, P. Xi, L. Tang, Y. Zhang, Y. Liu, S. Tan, L. Chen, *Nat. Biotechnol.* **2018**, *36*, 451.

[166] Z. Liu, S. Durant, H. Lee, Y. Pikus, N. Fang, Y. Xiong, C. Sun, X. Zhang, *Nano Lett.* **2007**, *7*, 403.

[167] Y. Xiong, Z. Liu, C. Sun, X. Zhang, *Nano Lett.* **2007**, *7*, 3360.

[168] L. Tian, L. Waller, *Optica* **2015**, *2*, 104.

[169] P. C. Konda, L. Loetgering, K. C. Zhou, S. Xu, A. R. Harvey, R. Horstmeyer, *Opt. Express* **2020**, *28*, 9603.

[170] V. Mico, J. J. Zheng, J. Garcia, Z. Zalevsky, P. Gao, *Adv. Opt. Photonics* **2019**, *11*, 135.

[171] X. Jiang, Q. Song, L. Xu, J. Fu, L. Tong, *Appl. Phys. Lett.* **2007**, *90*, 233501.

[172] D. Axelrod, *Traffic* **2001**, *2*, 764.

[173] D. R. Stabley, T. Oh, S. M. Simon, A. L. Mattheyses, K. Salaita, *Nat. Commun.* **2015**, *6*, 8307.

[174] J. Boulanger, C. Gueudry, D. Muench, B. Cinquin, P. Paul-Gilloteaux, S. Bardin, C. Guerin, F. Senger, L. Blanchoin, J. Salamero, *Proc. Natl. Acad. Sci. USA* **2014**, *111*, 17164.

[175] D. Axelrod, *J. Cell Biol.* **1981**, *89*, 141.

[176] J. Tian, Z. Ma, Q. A. Li, Y. Song, Z. H. Liu, Q. Yang, C. L. Zha, J. Akerman, L. M. Tong, M. Qiu, *Appl. Phys. Lett.* **2010**, *97*, 3.

[177] D. J. Sirbuly, A. Tao, M. Law, R. Fan, P. Yang, *Adv. Mater.* **2007**, *19*, 61.

[178] O. Frazao, J. L. Santos, F. M. Araujo, L. A. Ferreira, *Laser Photonics Rev.* **2008**, *2*, 449.

[179] J. B. Jensen, L. H. Pedersen, P. E. Hoiby, L. B. Nielsen, T. P. Hansen, J. R. Folkenberg, J. Riishede, D. Noordegraaf, K. Nielsen, A. Carlsen, A. Bjarklev, *Opt. Lett.* **2004**, *29*, 1974.

[180] N. P. Mauranyapin, L. S. Madsen, M. A. Taylor, M. Waleed, W. P. Bowen, *Nat. Photonics* **2017**, *11*, 477.

[181] S. Gaugiran, S. Getin, J. M. Fedeli, G. Colas, A. Fuchs, F. Chatelain, J. Derouard, *Opt. Express* **2005**, *13*, 6956.

[182] A. H. Yang, S. D. Moore, B. S. Schmidt, M. Klug, M. Lipson, D. Erickson, *Nature* **2009**, *457*, 71.

[183] Y. F. Chen, X. Serey, R. Sarkar, P. Chen, D. Erickson, *Nano Lett.* **2012**, *12*, 1633.

[184] P. Xu, S. Liu, M. Tang, X. Xu, X. Lin, Z. Wu, M. ZhuGe, Z. Ren, Z. Wang, X. Liu, Z. Yang, N. Raghavan, Q. Yang, *Appl. Phys. Lett.* **2017**, *110*, 201112.

[185] M. Tang, P. Xu, Z. Wen, X. Chen, C. Pang, X. Xu, C. Meng, X. Liu, H. Tian, N. Raghavan, Q. Yang, *Sci. Bull.* **2018**, *63*, 1118.

[186] X. F. Duan, Y. Huang, R. Agarwal, C. M. Lieber, *Nature* **2003**, *421*, 241.

[187] X. Xu, X. Liu, C. Pang, Y. Ma, C. Meng, J. Zhang, X. Liu, Q. Yang, *J. Phys. D: Appl. Phys.* **2019**, *52*, 284002.

[188] F. Ströhl, I. S. Opstad, J.-C. Tinguely, F. T. Dullo, I. Mela, J. W. M. Osterrieth, B. S. Ahluwalia, C. F. Kaminski, *Opt. Express* **2019**, *27*, 25280.

[189] Y. Chen, W. Liu, Z. Zhang, C. Zheng, Y. Huang, R. Cao, D. Zhu, L. Xu, M. Zhang, Y.-H. Zhang, J. Fan, L. Jin, Y. Xu, C. Kuang, X. Liu, *Nat. Commun.* **2018**, *9*, 4818.

[190] M. Muller, V. Monkemoller, S. Hennig, W. Hubner, T. Huser, *Nat. Commun.* **2016**, *7*, 10980.

[191] R. Heintzmann, T. Huser, *Chem. Rev.* **2017**, *117*, 13890.

[192] B.-J. Chang, S. H. Lin, L.-J. Chou, S.-Y. Chiang, *Opt. Lett.* **2011**, *36*, 4773.

[193] K. Wicker, R. Heintzmann, *Nat. Photonics* **2014**, *8*, 342.

[194] A. Lal, C. Shan, P. Xi, *IEEE J. Sel. Top. Quantum Electron.* **2016**, *22*, 50.

[195] K. Wicker, *Opt. Express* **2013**, *21*, 24692.

**ADVANCED
SCIENCE NEWS**

www.advancedsciencenews.com

LASER
& PHOTONICS
REVIEWS

www.lpr-journal.org

[196] K. Wicker, O. Mandula, G. Best, R. Fiolka, R. Heintzmann, *Opt. Express* **2013**, *21*, 2032.

[197] V. Perez, B. J. Chang, E. H. Stelzer, *Sci. Rep.* **2016**, *6*, 37149.

[198] R. Cao, Y. Chen, W. Liu, D. Zhu, C. Kuang, Y. Xu, X. Liu, *Biomed. Opt. Express* **2018**, *9*, 5037.

[199] J. L. Ponsetto, F. Wei, Z. Liu, *Nanoscale* **2014**, *6*, 5807.

[200] A. Bezryadina, J. Zhao, Y. Xia, Y. U. Lee, X. Zhang, Z. Liu, *Opt. Lett.* **2019**, *44*, 2915.

[201] C. B. Müller, J. Enderlein, *Phys. Rev. Lett.* **2010**, *104*, 198101.

[202] S. Roth, C. J. R. Sheppard, K. Wicker, R. Heintzmann, *Opt. Nanosc.* **2013**, *2*, 5.

[203] A. G. York, S. H. Parekh, D. Dalle Nogare, R. S. Fischer, K. Temprine, M. Mione, A. B. Chitnis, C. A. Combs, H. Shroff, *Nat. Methods* **2012**, *9*, 749.

[204] E. Chung, D. Kim, P. T. So, *Opt. Lett.* **2006**, *31*, 945.

[205] D. Li, L. Shao, B.-C. Chen, X. Zhang, M. Zhang, B. Moses, D. E. Milkie, J. R. Beach, J. A. Hammer, M. Pasham, *Science* **2015**, *349*, aab3500.

[206] R. Förster, H.-W. Lu-Walther, A. Jost, M. Kielhorn, K. Wicker, R. Heintzmann, *Opt. Express* **2014**, *22*, 20663.

[207] L. J. Young, F. Strohl, C. F. Kaminski, *J. Visualized Exp.* **2016**, *30*, 53988.

[208] J. Nixon-Abell, C. J. Obara, A. V. Weigel, D. Li, W. R. Legant, C. S. Xu, H. A. Pasolli, K. Harvey, H. F. Hess, E. Betzig, C. Blackstone, J. Lippincott-Schwartz, *Science* **2016**, *354*, aaf3928.

[209] G. Jellison, Jr., *Opt Mater.* **1992**, *1*, 151.

[210] J. C. Tinguely, O. I. Helle, B. S. Ahluwalia, *Opt. Express* **2017**, *25*, 27678.

[211] Y. Fu, T. Ye, W. Tang, T. Chu, *Photonics Res.* **2014**, *2*, A41.

[212] S. A. Maier, *Plasmonics: Fundamentals and Applications*, Springer, New York **2007**.

[213] W. L. Barnes, A. Dereux, T. W. Ebbesen, *Nature* **2003**, *424*, 824.

[214] A. V. Zayats, I. I. Smolyaninov, A. A. Maradudin, *Phys. Rep.* **2005**, *408*, 131.

[215] K. A. Willets, A. J. Wilson, V. Sundaresan, P. B. Joshi, *Chem. Rev.* **2017**, *117*, 7538.

[216] B. Simkhovich, G. Bartal, *Phys. Rev. Lett.* **2014**, *112*, 056802.

[217] S. Kawata, Y. Inouye, P. Verma, *Nat. Photonics* **2009**, *3*, 388.

[218] M. Li, S. K. Cushing, N. Wu, *Analyst* **2015**, *140*, 386.

[219] O. Krupin, W. R. Wong, F. R. Mahamd Adikan, P. Berini, *IEEE J. Sel. Top. Quantum Electron.* **2017**, *23*, 103.

[220] P. Singh, *Sens. Actuators, B* **2016**, *229*, 110.

[221] B. Spackova, P. Wrobel, M. Bockova, J. Homola, *Proc. IEEE* **2016**, *104*, 2380.

[222] M. Soler, M. C. Estevez, R. Villar-Vazquez, J. I. Casal, L. M. Lechuga, *Anal. Chim. Acta* **2016**, *930*, 31.

[223] F. Yesilkoy, R. A. Terborg, J. Pello, A. A. Belushkin, Y. Jahani, V. Pruneri, H. Altug, *Light: Sci. Appl.* **2018**, *7*, 17152.

[224] A. A. Rifat, R. Ahmed, G. A. Mahdiraji, F. R. M. Adikan, *IEEE Sens. J.* **2017**, *17*, 2776.

[225] P. Zijlstra, P. M. Paulo, M. Orrit, *Nat. Nanotechnol.* **2012**, *7*, 379.

[226] J. N. Anker, W. P. Hall, O. Lyandres, N. C. Shah, J. Zhao, R. P. Van Duyne, *Nat. Mater.* **2008**, *7*, 442.

[227] S. Schlucker, *Angew. Chem., Int. Ed. Engl.* **2014**, *53*, 4756.

[228] K. Saha, S. S. Agasti, C. Kim, X. Li, V. M. Rotello, *Chem. Rev.* **2012**, *112*, 2739.

[229] H. Lu, X. Gan, D. Mao, J. Zhao, *Photonics Res.* **2017**, *5*, 162.

[230] D. K. Gramotnev, S. I. Bozhevolnyi, *Nat. Photonics* **2010**, *4*, 83.

[231] V. A. Zenin, S. Choudhury, S. Saha, V. M. Shalaev, A. Boltasseva, S. I. Bozhevolnyi, *Opt. Express* **2017**, *25*, 12295.

[232] F. Vetrone, F. Rosei, *Science* **2017**, *357*, 452.

[233] Y. Wang, Y. Ma, X. Guo, L. Tong, *Opt. Express* **2012**, *20*, 19006.

[234] J. Luo, B. Zeng, C. Wang, P. Gao, K. Liu, M. Pu, J. Jin, Z. Zhao, X. Li, H. Yu, X. Luo, *Nanoscale* **2015**, *7*, 18805.

[235] P. Gao, N. Yao, C. Wang, Z. Zhao, Y. Luo, Y. Wang, G. Gao, K. Liu, C. Zhao, X. Luo, *Appl. Phys. Lett.* **2015**, *106*, 093110.

[236] G. Liang, X. Chen, Q. Zhao, L. J. Guo, *Nanophotonics* **2018**, *7*, 277.

[237] K. Cheng, Y. Q. Wu, J. Meng, Y. L. Zhao, X. Y. Wang, Z. L. Du, *Sci. Bull.* **2015**, *60*, 541.

[238] H. A. Atwater, A. Polman, *Nat. Mater.* **2010**, *9*, 205.

[239] S. Linic, P. Christopher, D. B. Ingram, *Nat. Mater.* **2011**, *10*, 911.

[240] J. A. Schuller, E. S. Barnard, W. Cai, Y. C. Jun, J. S. White, M. L. Brongersma, *Nat. Mater.* **2010**, *9*, 193.

[241] C. Bradac, *Adv. Opt. Mater.* **2018**, *6*, 1800005.

[242] D. Gao, W. Ding, M. Nieto-Vesperinas, X. Ding, M. Rahman, T. Zhang, C. Lim, C.-W. Qiu, *Light: Sci. Appl.* **2017**, *6*, 17039.

[243] V. Garces-Chavez, R. Quidant, P. J. Reece, G. Badenes, L. Torner, K. Dholakia, *Phys. Rev. B* **2006**, *73*, 5.

[244] G. Volpe, R. Quidant, G. Badenes, D. Petrov, *Phys. Rev. Lett.* **2006**, *96*, 238101.

[245] Y. Pang, R. Gordon, *Nano Lett.* **2012**, *12*, 402.

[246] A. N. Grigorenko, N. W. Roberts, M. R. Dickinson, Y. Zhang, *Nat. Photonics* **2008**, *2*, 365.

[247] T. Zhu, Y. Zhou, Y. Lou, H. Ye, M. Qiu, Z. Ruan, S. Fan, *Nat. Commun.* **2017**, *8*, 15391.

[248] Z. C. Ruan, *Opt. Lett.* **2015**, *40*, 601.

[249] A. Pors, M. G. Nielsen, S. I. Bozhevolnyi, *Nano Lett.* **2015**, *15*, 791.

[250] A. Silva, F. Monticone, G. Castaldi, V. Galdi, A. Alu, N. Engheta, *Science* **2014**, *343*, 160.

[251] N. Fang, H. Lee, C. Sun, X. Zhang, *Science* **2005**, *308*, 534.

[252] Z. Liu. *Plasmonics and Super-Resolution Imaging*, Jenny Stanford Publishing, Singapore **2017**.

[253] X. G. Luo, D. P. Tsai, M. Gu, M. H. Hong, *Adv. Opt. Photonics* **2018**, *10*, 757.

[254] E. N. Economou, *Phys. Rev.* **1969**, *182*, 539.

[255] Q. Wang, J. Bu, P. Tan, G. Yuan, J. H. Teng, H. Wang, X.-C. Yuan, *Plasmonics* **2012**, *7*, 427.

[256] P. Tan, X.-C. Yuan, G. Yuan, Q. Wang, *Appl. Phys. Lett.* **2010**, *97*, 241109.

[257] S. Wei, T. Lei, L. Du, C. Zhang, H. Chen, Y. Yang, S. Zhu, X.-C. Yuan, *Opt. Express* **2015**, *23*, 30143.

[258] C. Zhang, C. Min, L. Du, X. C. Yuan, *Appl. Phys. Lett.* **2016**, *108*, 201601.

[259] N. Chakrova, R. Heintzmann, B. Rieger, S. Stallinga, *Opt. Express* **2015**, *23*, 31367.

[260] Z. Liu, Y. Wang, J. Yao, H. Lee, W. Srituravanich, X. Zhang, *Nano Lett.* **2009**, *9*, 462.

[261] I. Avrutsky, I. Salakhutdinov, J. Elser, V. Podolskiy, *Phys. Rev. B* **2007**, *75*, 241402.

[262] Y. Xiong, Z. Liu, X. Zhang, *Appl. Phys. Lett.* **2008**, *93*, 111116.

[263] S. Cao, T. Wang, W. Xu, H. Liu, H. Zhang, B. Hu, W. Yu, *Sci. Rep.* **2016**, *6*, 23460.

[264] S. Cao, T. Wang, J. Yang, B. Hu, U. Levy, W. Yu, *Sci. Rep.* **2017**, *7*, 1328.

[265] K. S. Novoselov, A. K. Geim, S. V. Morozov, D. Jiang, Y. Zhang, S. V. Dubonos, I. V. Grigorieva, A. A. Firsov, *Science* **2004**, *306*, 666.

[266] K. S. Novoselov, A. K. Geim, S. V. Morozov, D. Jiang, M. I. Katsnelson, I. V. Grigorieva, S. V. Dubonos, A. A. Firsov, *Nature* **2005**, *438*, 197.

[267] A. K. Geim, K. S. Novoselov, *Nat. Mater.* **2007**, *6*, 183.

[268] X. Z. Liu, T. Galfsky, Z. Sun, F. N. Xia, E. C. Lin, Y. H. Lee, S. Kena-Cohen, V. M. Menon, *Nat. Photonics* **2015**, *9*, 30.

[269] Y. F. Dong, Z. S. Wu, W. C. Ren, H. M. Cheng, X. H. Bao, *Sci. Bull.* **2017**, *62*, 724.

[270] C. Pang, H. Lu, P. Xu, H. Qian, X. Liu, X. Liu, H. Li, Q. Yang, *Opt. Express* **2016**, *24*, 17069.

[271] P. Xu, H. Zhang, H. Qian, B. Chen, X. Jiang, Y. Wu, X. Liu, X. Liu, Q. Yang, *Opt. Commun.* **2017**, *395*, 76.

[272] H. Qian, Y. Ma, Q. Yang, B. Chen, Y. Liu, X. Guo, S. Lin, J. Ruan, X. Liu, L. Tong, Z. L. Wang, *ACS Nano* **2014**, *8*, 2584.

[273] T. Low, P. Avouris, *ACS Nano* **2014**, *8*, 1086.

[274] M. Tymchenko, A. Y. Nikitin, L. Martin-Moreno, *ACS Nano* **2013**, *7*, 9780.

[275] H. Hu, X. Yang, F. Zhai, D. Hu, R. Liu, K. Liu, Z. Sun, Q. Dai, *Nat. Commun.* **2016**, *7*, 12334.

[276] L. Huang, J. Liu, H. Deng, S. Wu, *Adv. Opt. Mater.* **2018**, *6*, 1701378.

[277] A. Vakil, N. Engheta, *Science* **2011**, *332*, 1291.

[278] R. R. Zhang, X. Lin, L. Shen, Z. J. Wang, B. Zheng, S. S. Lin, H. S. Chen, *Opt. Lett.* **2014**, *39*, 6739.

[279] J. Yang, T. Wang, Z. Chen, B. Hu, W. Yu, *Sci. Rep.* **2016**, *6*, 37898.

[280] S. Cao, T. Wang, Q. Sun, B. Hu, U. Levy, W. Yu, *Opt. Express* **2017**, *25*, 14494.

[281] B. H. Cheng, K. J. Chang, Y. C. Lan, D. P. Tsai, *Opt. Express* **2014**, *22*, 28635.

[282] L. Ju, B. S. Geng, J. Horng, C. Girit, M. Martin, Z. Hao, H. A. Bechtel, X. G. Liang, A. Zettl, Y. R. Shen, F. Wang, *Nat. Nanotechnol.* **2011**, *6*, 630.

[283] I. V. Iorsh, I. S. Mukhin, I. V. Shadrivov, P. A. Belov, Y. S. Kivshar, *Phys. Rev. B* **2013**, *87*, 075416.

[284] N. M. Idris, M. K. Gnanasammandhan, J. Zhang, P. C. Ho, R. Mahendran, Y. Zhang, *Nat. Med.* **2012**, *18*, 1580.

[285] M. He, X. Pang, X. Liu, B. Jiang, Y. He, H. Snaith, Z. Lin, *Angew. Chem., Int. Ed. Engl.* **2016**, *55*, 4280.

[286] S. Ishii, A. V. Kildishev, E. Narimanov, V. M. Shalaev, V. P. Drachev, *Laser Photonics Rev.* **2013**, *7*, 265.

[287] F. Liu, L. Xiao, Y. Ye, M. Wang, K. Cui, X. Feng, W. Zhang, Y. Huang, *Nat. Photonics* **2017**, *11*, 289.

[288] J. S. T. Smalley, F. Vallini, X. Zhang, Y. Fainman, *Adv. Opt. Photonics* **2018**, *10*, 354.

[289] Y. Chen, *Microelectron. Eng.* **2015**, *135*, 57.

[290] C.-S. Kim, S.-H. Ahn, D.-Y. Jang, *Vacuum* **2012**, *86*, 1014.

[291] H. O. Moser, C. Rockstuhl, *Laser Photonics Rev.* **2012**, *6*, 219.

[292] M. Hauser, M. Wojcik, D. Kim, M. Mahmoudi, W. Li, K. Xu, *Chem. Rev.* **2017**, *117*, 7428.

[293] D. P. Hoffman, G. Shtengel, C. S. Xu, K. R. Campbell, M. Freeman, L. Wang, D. E. Milkie, H. A. Pasolli, N. Iyer, J. A. Bogovic, D. R. Stabley, A. Shirinifard, S. Pang, D. Peale, K. Schaefer, W. Pomp, C.-L. Chang, J. Lippincott-Schwartz, T. Kirchhausen, D. J. Solecki, E. Betzig, H. F. Hess, *Science* **2020**, *367*, eaaz5357.

[294] R. Diekmann, Ø. I. Helle, C. I. Øie, P. McCourt, T. R. Huser, M. Schüttpelz, B. S. Ahluwalia, *Nat. Photonics* **2017**, *11*, 322.

[295] Y. Rivenson, Z. Göröcs, H. Günaydin, Y. Zhang, H. Wang, A. Ozcan, *Optica* **2017**, *4*, 1437.

[296] H. Wang, Y. Rivenson, Y. Jin, Z. Wei, R. Gao, H. Gunaydin, L. A. Bentolila, C. Kural, A. Ozcan, *Nat. Methods* **2019**, *16*, 103.

[297] Y. Rivenson, H. Ceylan Koydemir, H. Wang, Z. Wei, Z. Ren, H. Günaydın, Y. Zhang, Z. Göröcs, K. Liang, D. Tseng, A. Ozcan, *ACS Photonics* **2018**, *5*, 2354.

[298] Q. Wei, H. Qi, W. Luo, D. Tseng, S. J. Ki, Z. Wan, Z. Göröcs, L. A. Bentolila, T.-T. Wu, R. Sun, A. Ozcan, *ACS Nano* **2013**, *7*, 9147.

[299] H. Zhu, S. O. Isikman, O. Mudanyali, A. Greenbaum, A. Ozcan, *Lab Chip* **2013**, *13*, 51.

[300] A. E. Cetin, A. F. Coskun, B. C. Galarreta, M. Huang, D. Herman, A. Ozcan, H. Altug, *Light: Sci. Appl.* **2014**, *3*, e122.

[301] D. O. S. Melville, R. J. Blaikie, *Opt. Express* **2005**, *13*, 2127.

[302] V. Westphal, S. O. Rizzoli, M. A. Lauterbach, D. Kamin, R. Jahn, S. W. Hell, *Science* **2008**, *320*, 246.

[303] F. Huang, T. M. P. Hartwich, F. E. Rivera-Molina, Y. Lin, W. C. Duim, J. J. Long, P. D. Uchil, J. R. Myers, M. A. Baird, W. Mothes, M. W. Davidson, D. Toomre, J. Bewersdorf, *Nat. Methods* **2013**, *10*, 653.

[304] P. Kner, B. B. Chhun, E. R. Griffis, L. Winoto, M. G. Gustafsson, *Nat. Methods* **2009**, *6*, 339.

[305] K. F. Sonnen, L. Schermelleh, H. Leonhardt, E. A. Nigg, *Biol. Open* **2012**, *1*, 965.

[306] L. Shao, P. Kner, E. H. Rego, M. G. Gustafsson, *Nat. Methods* **2011**, *8*, 1044.

[307] A. Classen, J. von Zanthier, M. O. Scully, G. S. Agarwal, *Optica* **2017**, *4*, 580.

Mingwei Tang is currently a Ph.D. student at the College of Optical Science and Engineering, Zhejiang University, Hangzhou, China, under the supervision of Qing Yang. His current research interests involve the field of nanomaterials, metamaterials, and their applications in superresolution imaging and sensing in medical cell biology.

Xu Liu received his D.Sc. degree from L'Ecole Nationale Supérieure de Physique de Marseille in France. He has been a professor in the College of Optical Science and Engineering at Zhejiang University since 1995. His research interests include the optoelectronic display, optics and optoelectronic thin films, optical imaging (including new imaging technologies such as superresolution imaging, computational imaging, and high-speed spectral imaging), and biooptical technologies. He is also a COS (the Chinese Optical Society) fellow and OSA (the Optical Society of America) fellow.

Yaoguang Ma received his Ph.D. degree focusing on nanophotonic devices with Prof. Limin Tong at the College of Optical Science and Engineering from Zhejiang University in June 2012. After that, he has been a postdoc researcher at Peking University (PKU), University of California, San Diego (UCSD), and University of Colorado Boulder (CU Boulder). Since January 2018, he started his faculty career as a tenure-track professor at Zhejiang University. His research interests are in the fundamentals of nanoscale light–matter interactions and the converged applications of nanotechnologies in modern optical systems.

Qing Yang received her Ph.D. degree in materials science and engineering from Zhejiang University in 2006. She worked as a visiting scientist in material science and engineering at Georgia Institute of Technology from 2009 to 2012. Currently, she is a professor in the College of Optical Science and Engineering at Zhejiang University. Her research focuses on micro/nanophotonics, piezo-phototronics, and flexible nanosystems.